

# **First Steps Toward the Construction of a Channel Cell for Electrochemical Studies under Hydrothermal Conditions**

by

Fereshteh Samiee

A Thesis Submitted in Partial Fulfillment of the  
Requirements for the Degree of  
Master in Materials Science

University of Ontario Institute of Technology  
Faculty of Science  
August 2015

© Fereshteh Samiee 2015

## Abstract

This thesis constitutes the first step in the design and construction of a high- temperature and high-pressure channel flow cell (HT-CFC) for electrochemical studies under hydrothermal conditions. The system would allow to investigate at a fundamental level the interaction between new materials and media conditions such those found in modern power plants, industrial processes, and geochemistry.

A first CFC prototype was constructed based on the evaluation of different room temperature cell designs, and the performance of the cell was studied using the oxidation of ferrocyanide in 0.1M KCl as reference system under room temperature conditions. A numerical simulation software, COMSOL Multiphysics, was used to analyze the experimental results, as well as to evaluate other cell/electrode configurations that could perform better under hydrothermal conditions.

At the same time, the thermal stability of hydroquinone ( $H_2Q$ ) and 1,4-benzoquinone (BQ), a redox couple that it could be used to extend the evaluation of the CFC to higher temperatures and pressures was also investigated using UV-visible spectroscopy up to 250 °C at 70 bar. These studies confirmed  $H_2Q$  is stable in hot compressed water (pH ~ 2) up to at least 250 °C at 70 bar, but BQ, the oxidation production of  $H_2Q$ , decomposes at temperatures lower than 100 °C with the formation  $H_2Q$  and other non-absorbing products. Based on these results, the oxidation of  $H_2Q$  to BQ in acid media could fulfill the stability requirements for the evaluation of a future HT-CFC provided that BQ be removed from the cell before it undergoes decomposition.

**Keywords:** Hydrodynamic electrodes, channel flow cell, UV-visible spectroscopy, hydrothermal systems, hydroquinone, 1,4-benzoquinone, COMSOL Multiphysics, numerical simulations.

## Contents

Contents .....	iv
List of Figures .....	vi
List of Tables .....	viii
Abbreviations and Physical Constants .....	ix
Acknowledgements .....	xi
<b>Chapter 1: Introduction.....</b>	<b>1</b>
1.1 Electrochemistry in Hydrothermal Systems .....	1
1.2 High T,p Electrochemical Studies without Forced Convection .....	3
1.3 High T,p Electrochemical Studies using Hydrodynamic Electrodes.....	4
1.3.1 Rotating Disc Electrode System (HT-RDE) .....	4
1.3.2 Imping Jet Electrode Systems .....	6
1.3.3 Annular-Duct and Channel Cell Electrodes .....	7
1.4 Reference Electrodes for High Temperature Studies .....	8
1.5 Aims and Objectives.....	9
1.6 Thesis Outline.....	9
<b>Chapter 2: Fundamental Concepts and Terminology .....</b>	<b>11</b>
2.1 Electron Transfer and Mass Transport in Solution.....	11
2.2 Diffusion Current: The Second Fick's Law .....	12
2.3 Theoretical Treatment of Convective Systems.....	13
2.3.1 Channel Flow Cell: Diffusion-Convection Equation .....	13
2.3.2 Determination of Velocity Profile.....	16
2.4 Numerical Simulation .....	17
2.4.1 Finite Element Analysis .....	18
2.4.2 Simulations Using COMSOL MP .....	18
<b>Chapter 3: HT-CFC Design Optimization using a Numerical Simulation Method</b>	
<b>.....</b>	<b>21</b>
3.1 Introduction.....	21
3.2 Experimental Section.....	22
3.2.1 Chemicals and Materials .....	22
3.2.2 Electrochemical Experiments.....	23
3.2.3 CFC: Room Temperature Prototype .....	23

3.3	Numerical simulations .....	25
3.3.1	COMSOL MP Model .....	25
3.4	Results and Discussion .....	27
3.4.1	Electrochemical Studies-Cell Evaluation .....	27
3.4.2	Evaluation of Numerical Simulation Results .....	30
3.4.3	First Steps Toward the Construction of an HT-CFC.....	39
3.5	Conclusions .....	42
<b>Chapter 4: Redox Couples for High T,p Electrochemical Studies .....</b>		<b>43</b>
4.1	Introduction.....	43
4.2	Experimental Section.....	44
4.2.1	Chemicals .....	44
4.2.2	High T,p UV-visible Spectroscopic Cell and Injection System.....	45
4.2.3	Procedure Adopted for Collecting the Absorption Spectra.....	47
4.2.4	Analysis of the Spectroscopic Data.....	48
4.3	Results and Discussion .....	49
4.3.1	Temperature and Pressure Effects on the Spectrum of BQ.....	51
4.3.2	Temperature and Pressure Effects on the Spectrum of HQ .....	53
4.3.3	Mechanism of Decomposition and Formation of Other Species.....	54
4.4	Conclusions .....	56
<b>Chapter 5: Conclusions and Future Work .....</b>		<b>57</b>
References .....		59
Appendix A: Copyright permission .....		67

## List of Figures

Figure 1-1: Temperature and pressure dependence of: (a) density and (b) dielectric constant of water (REFPROP, version 8, NIST). .....	2
Figure 1-2: Schematic diagram of the RDE with the corresponding flow profile.....	4
Figure 1-3: Schematic of a HT-RDE. Reproduced from [12], Copyright 2015, with permission from AIP.....	5
Figure 1-4: Wall-tube electrode (nozzle diameter $\gg$ electrode diameter) [28]. .....	6
Figure 2-1: A schematic representation of a simple electrochemical process. ....	11
Figure 2-2: Concentration profile and diffusion layer approximation (dashed lines). $x=0$ corresponds to the electrode surface, and $\delta_0$ is the diffusion layer thickness. ....	13
Figure 2-3: Possible flow pattern in a pipe or channel: (a)Turbulent flow, (b)Laminar flow [25].....	17
Figure 2-4: Finite element simulation method used in COMSOL MP to predict linear sweep voltammetry results in a channel flow cell. ....	20
Figure 3-1: Channel Flow Cell (CFC) dimensions. ....	21
Figure 3-2: (a) Schematic diagram of the room temperature CFC: (A) cell body; (B) electrode support; (C) o’ring; (D) bolted end-cap; (E) inlet; (F) outlet and (G) Pt working electrode; (b) picture of the cell after assembling. ....	24
Figure 3-3: Physical descriptions of the channel and electrode ( $2h=1\text{ mm}$ , $d=4\text{ mm}$ , $l=40\text{ mm}$ ). .....	25
Figure 3-4: (a) Linear sweep voltammograms for the oxidation of 1.5 mM ferrocyanide in 0.1 M KCl obtained using a RDE at different rotation rates (scan rate: $20\text{ mV}\cdot\text{s}^{-1}$ ), (b) Levich’s plot for the same.....	28
Figure 3-5: (a) Linear sweep voltammograms for the oxidation of 0.95 mM ferrocyanide and reduction of 1.27 mM ferricyanide in 0.2 M KCl in a CFC at different flow rates (scan rate: $20\text{ mV}\cdot\text{s}^{-1}$ ), (b) Levich plot ( $i_L$ vs $V_f^{1/3}$ ) for the oxidation of ferrocyanide. ....	29
Figure 3-6: Diffusion layer thickness in a CFC vs. volume flow rate. ....	30
Figure 3-7: Limiting current density for the oxidation of 0.95 mM ferrocyanide for a band electrode ( $w=4\text{ mm}$ , $x_e=1\text{ mm}$ , $2h=1\text{ mm}$ ) at $V_f$ values of 6,10,14,18 $\text{cm}^3\cdot\text{min}^{-1}$ . ..	31
Figure 3-8: CFC user defined meshing (manual): (a) 3D channel cell meshing, (b) zy plane at the corner of electrode, (c) yx plane ate at the surface of electrode. ....	33
Figure 3-9: CFC user defined meshing (manual): (a) 3D channel cell meshing, (b) zy plane at the corner of electrode, (c) yx plane ate at the surface of electrode. ....	33

Figure 3-10: comparison between different meshing, users defined meshing with higher granularity and auto-meshing for a band electrode.....	34
Figure 3-11: (a) Limiting current for the oxidation of 0.95 mM ferrocyanide, (b) Comparison of the simulated $I_{lim}$ (○) to the Levich equation (–) and the experimental data (●) for a band electrode ( $w=4\text{mm}$ , $x_e=1\text{mm}$ , $2h=1\text{mm}$ ) at $20\text{ mV}\cdot\text{min}^{-1}$ at $V_f$ values of 6,10,14,18 $\text{cm}^3\cdot\text{min}^{-1}$ .....	35
Figure 3-12: Velocity profile obtained by solving Navier-Stokes equation under laminar flow condition ( $V_f = 8\text{cm}^3\cdot\text{min}^{-1}$ ).....	36
Figure 3-13: Viscosity of water vs. temperature plot at several pressures (Data were taken from REFPROP (version 8)-NIST).....	37
Figure 3-14: Concentration profile on the surface of electrode and diffusion layer thickness.....	38
Figure 3-15: (a) Concentration gradient ( $\text{mol}\cdot\text{cm}^{-3}$ ) of electroactive species at the surface of electrode, at $18\text{ cm}^3\cdot\text{min}^{-1}$ compared with (b) concentration profile obtained by Compton et al. [28]. .....	38
Figure 4-1: UV-visible flow cell and high-pressure injection system, (1) solution, (2) nitrogen balloon, (3) peristaltic pump, (4) six port valve, (5) PEEK injection loop, (6) nitrogen gas, (7) deionized water, (8) HPLC pump, (9) waste, (10) titanium preheater, (11) titanium cell, (12) outlet, (13) waste, (14) heater, and (15) ceramic insulation...	46
Figure 4-2: Picture of the high T,p UV-Vis spectroscopy system used for studying the thermal stability of $\text{H}_2\text{Q}$ and BQ.....	46
Figure 4-3: Baseline-corrected absorbance data for 0.3 mM $\text{H}_2\text{Q}$ in 0.2M $\text{NaHSO}_4$ at $100^\circ\text{C}$ in titanium cell. Arrows indicate the evaluation of the spectra upon time after injection.....	47
Figure 4-4: Normalized UV-visible absorption spectra for 0.07 mM BQ (top) and 0.3 mM $\text{H}_2\text{Q}$ (bottom) in 0.2M $\text{NaHSO}_4$ at 25, 100, 150, and 200 $^\circ\text{C}$ and 70 bar. The spectrum for $\text{H}_2\text{Q}$ at $250^\circ\text{C}$ and 70 bar (broken blue line) was also included. ....	50
Figure 4-5: Normalized UV-visible absorption spectra for 0.07 mM BQ: Blue shift in the wavelength of the maximum absorbance with temperature (25, 100, 150, and 200 $^\circ\text{C}$ at 70 bar). ....	51
Figure 4-6: Difference spectra ( $A(T) - A(100^\circ\text{C})$ ) for 0.07 mM BQ in 0.2 M $\text{Na}_2\text{HSO}_4$ at 150, 200, and 200 $^\circ\text{C}$ and 70 bar. Reference spectrum: 0.07 mM BQ at 100 $^\circ\text{C}$ . Spectra corrected to account for thermal expansion of the solution. ....	53
Figure 4-7: Difference spectra ( $A(T) - A(100^\circ\text{C})$ ) for 0.3 mM $\text{H}_2\text{Q}$ in 0.2 M $\text{Na}_2\text{HSO}_4$ at 150, 200, and 200 $^\circ\text{C}$ and 70 bar. Reference spectrum: 0.03 mM BQ at 100 $^\circ\text{C}$ . Spectra corrected to account for thermal expansion of the solution. ....	54

## List of Tables

Table 3-1: Common CFC configuration in the bibliography.....	22
Table 3-2: Navier-Stokes and convection/diffusion transport equations and boundary conditions for numerical modeling. ....	26
Table 3-3: Diffusion coefficient, D, for $\text{Fe}(\text{CN})_6^{4-}$ as reported by other authors at 25°C. ....	27
Table 3-4: Meshing properties selected for the simulation of room temperature prototype CFC.....	32
Table 3-5: Calculated Reynolds numbers and diffusion layer thickness for hydroquinone at temperatures between 25 and 250 °C at 150 bar for a nominal volume flow rate at room temperature equal to $10 \text{ cm}^3 \cdot \text{min}^{-1}$ and two CFC configurations. ...	39
Table 3-6: Thermal expansion coefficient for potential materials as working electrode and electrode support. ....	41
Table 4-1: Density of water used to correct the absorption spectra.....	48
Table 4-2: Effect of dielectric constant of the solvent on the wavelength of the maximum of absorption fo BQ. ....	52

## Abbreviations and Physical Constants

---

<b>A(<math>\lambda</math>)</b>	Absorbance at wavelength $\lambda$	
<b>k<sub>B</sub></b>	Boltzmann constant	1.381x10 <sup>-23</sup> J·K <sup>-1</sup>
<b><math>\alpha_c</math></b>	Cathodic transfer coefficient	
<b>CFC</b>	Channel Flow Cell	
<b>z<sub>i</sub></b>	Charge of species i	
<b>C<sub>i</sub>, C<sub>i</sub>*</b>	Concentration (bulk solution) of species i	
<b>i</b>	Current	
<b>j</b>	Current density	
<b><math>\rho</math></b>	Density	
<b>D<sub>i</sub></b>	Diffusion coefficient of species i	
<b><math>\delta</math></b>	Diffusion layer thickness	
<b><math>\mu</math></b>	Dynamic viscosity	
<b>E</b>	Electrode potential	
<b>e</b>	Electron charge	1.62 × 10 <sup>-19</sup> C.mol <sup>-1</sup>
<b>l<sub>e</sub></b>	Entry length of fluid	
<b>F</b>	Faraday's Constant	96485 C.mol <sup>-1</sup>
<b>J<sub>i</sub></b>	Flux of species i	
<b>f</b>	Force	
<b>k<sub>f</sub></b>	Forward reaction rate	
<b>f</b>	Frequency	
<b>R</b>	Gas constant	8.314 J.mol <sup>-1</sup> .K <sup>-1</sup>
<b>h</b>	Half height of channel cell	
<b>HPLC</b>	High performance liquid chromatography	
<b>k<sub>o</sub></b>	Heterogeneous rate constant	
<b><math>\nu</math></b>	Kinematic viscosity	
<b>x<sub>e</sub></b>	Length of electrode	
<b>LSV</b>	Linear sweep voltammetry	
<b>v<sub>o</sub></b>	Maximum velocity at center of channel	
<b>v<sub>m</sub></b>	Mean flow velocity	
<b><math>\epsilon_i(\lambda)</math></b>	Molar absorptivity of species i at wavelength $\lambda$	



<b>n</b>	Number of electron
<b>b</b>	Optical path length
<b><math>\eta</math></b>	Overpotential
<b>p</b>	Pressure
<b>PTFE</b>	Polytetrafluoroethylene
<b>PEEK</b>	Polyetheretherketone
<b>a</b>	Radius of capillary nozzle
<b>k<sub>b</sub></b>	Reverse reaction rate
<b>R<sub>e</sub></b>	Reynolds number
<b>RDE</b>	Rotating Disk Electrode
<b>m<sub>i</sub><sup>*</sup></b>	Specific molality of species i (mol.kg <sup>-1</sup> of solution)
<b>T</b>	Temperature
<b>t</b>	Time
<b>I</b>	Total current
<b>v</b>	Velocity
<b>V<sub>f</sub></b>	Volume flow rate
<b>WJE</b>	Wall -Jet Electrode
<b>WTE</b>	Wall-Tube Electrode
<b><math>\lambda</math></b>	Wavelength
<b>d</b>	Width of channel
<b>w</b>	Width of electrode

---

## Acknowledgements

I acknowledge my supervisor Dr. Liliana Trevani for all her support and guidance from day one of this project. I am immensely grateful for this opportunity of working with her. I would also like to thank Professor E. Bradley Easton and Professor Igor Svishchev for accepting to be my advisory committee members.

I am also grateful to the Faculty of Science at the University of Ontario Institute of Technology for research support and laboratory infrastructure, the Natural Sciences and Engineering Research Council of Canada for funding this project, and CMC Microsystem for facilitating access to COMSOL Multiphysics.

I would like express my appreciation and thanks to everyone who assisted and supported me in completing this work. Particularly, Christopher Odetola and the rest of my group for providing friendly and helpful discussions during my project. Special thanks go to O’Rian Reid, who as an undergraduate research assistant, assembled the first high-pressure system and to Casey Gillen, who made possible the subsequent modifications.

I could not even begin to express properly my gratitude to my friends who have stayed by my side through both the good and bad times of this endeavor, but I will make a heartfelt attempt.

Last but never least, I would like to thank my lovely family, that even being away from me, was always supporting me.

# Chapter 1: Introduction

## 1.1 Electrochemistry in Hydrothermal Systems

Electrochemical systems able to operate over wide ranges of temperature and pressure conditions are required for the determination of temperature dependent properties such as standard electrode potentials, equilibrium constants, and transport properties in hydrothermal solutions. New electrochemical tools can also contribute to getting a better understanding of the mechanism of complex electrochemical processes and to the development of new materials and technologies for energy conversion and energy generation [1-3]. However, these experiments are challenging because both pressure and temperature must be controlled to keep the solvent in the liquid state. Figure 1-1(a) illustrates the changes in the density of water above and below the critical point ( $t_c = 373.95\text{ }^\circ\text{C}$  and  $p_c = 220.64\text{ bar}$ ) [4] and the single phase and two phases regions. Most of the electrochemical experiments over  $100\text{ }^\circ\text{C}$  have been carried out in pressurized static or flow cell autoclaves to keep the pressure of the system at or over the vapour pressure of water at each particular temperature, respectively. Another aspect that cannot be underestimated is the significant reduction in the dielectric constant of water with temperature at constant pressure (Figure 1-1 (b)), because it will impose significant solubility limitations as the temperature increases.

In terms of cell design, the experimental conditions are problematic because alloys such as stainless steel, that are extensively used at low temperatures because of its resistance to corrosion, can be attacked if glass or polymeric liners are not used [5]. The encapsulation of the working electrode is also a major problem because it is hard to find an electrode-support material with the same thermal expansion coefficient of the electrode material. If the difference is big then crevices will appear between the metal and the support. Finally, the contamination of the electrode surface by corrosion products and/or solutes decomposition products has shown to be a serious problem at temperatures over  $150\text{ }^\circ\text{C}$  [5, 6].

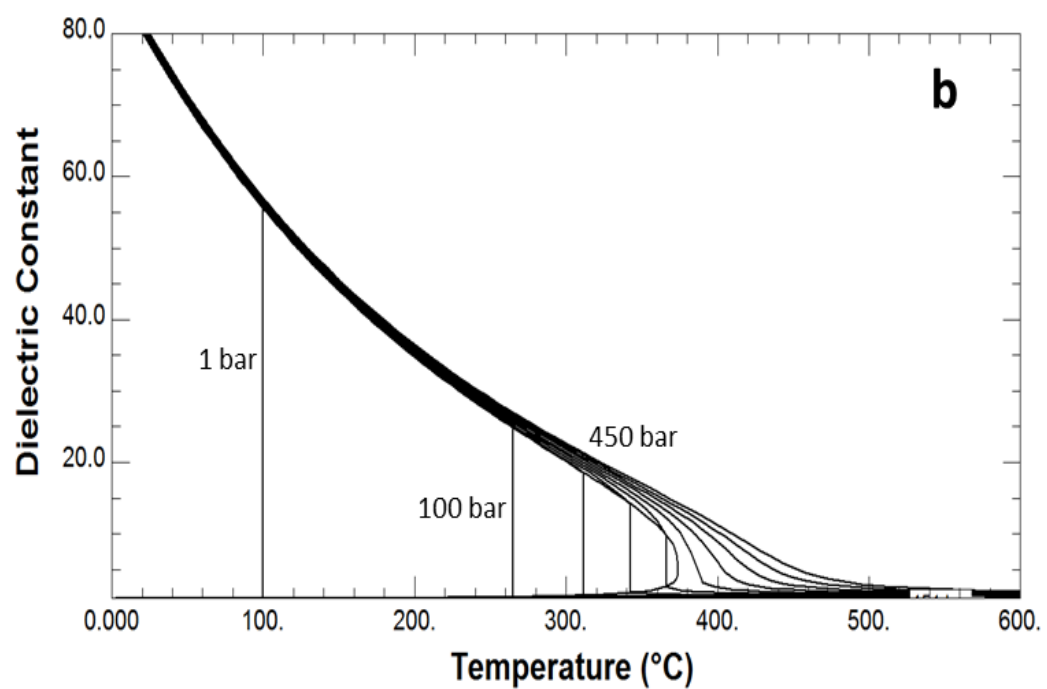
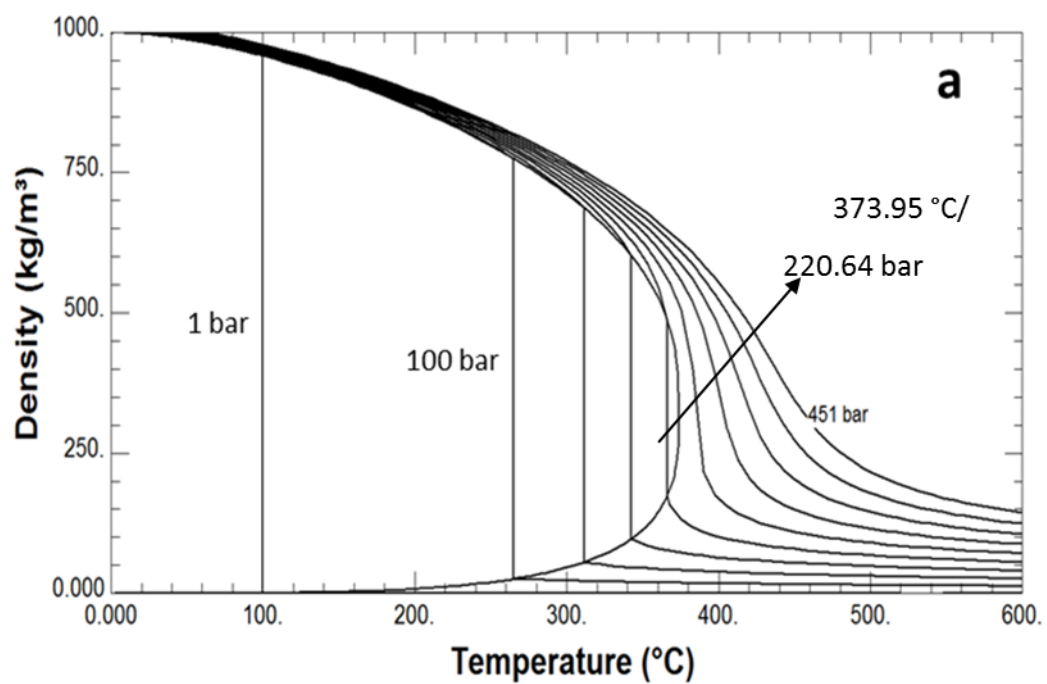


Figure 1-1: Temperature and pressure dependence of: (a) density and (b) dielectric constant of water (REFPROP, version 8, NIST).

The electrochemical studies performed at temperatures over 100 °C can be classified in different forms; one option is to group them based the way the electrode is heated:

- **Isothermal studies in autoclaves** where the electrode and the solution (static or flow system) are heated at high pressure [7-12]. A large number of these studies has been carried out using isothermal cells with the working (WE), reference (RE), and counter (CE) electrodes at the same temperature [1, 12-15]; however, other configurations, such as using an external reference electrode at room temperature are also common [16, 17]. The pro and cons of each configuration will be briefly discussed in Section 1.3.
- **Heated electrodes** where the interface electrode-solution is heated by heating the electrode, but the bulk solution remains under ambient conditions. The most representative examples in this group are the band microelectrodes heated by AC current developed by Grundle's and Baranski's groups [13, 18, 19] and the channel cell electrodes heated by radio frequency radiation [14, 15].

Because the focus of this thesis is electrochemistry on hydrothermal systems; only isothermal studies in autoclaves, static and flow systems, will be covered in the introduction.

## 1.2 High T,p Electrochemical Studies without Forced Convection

Systematic and detailed corrosion studies and pH measurements up to 350°C and 400 bar were carried out by MacDonald and Lvov [7, 20], but the studies involving static autoclaves [21] were slowly replaced by high-pressure flow systems and cells [9, 20]. Bard's group, a pioneer in the field of electrochemistry in supercritical fluids [5, 6, 10], made a major achievement while determining the diffusion coefficients of  $\text{Cu}^{2+}(\text{aq})$  [10],  $\text{H}_2\text{Q}$ , bromide and iodide [6] at temperatures and pressures close to the critical point of water. These studies involved the use of both, macro and microelectrodes, and the diffusion coefficients were obtained from chronoamperometric experiments in the absence of convection using the Cottrell equation [22].

### 1.3 High T,p Electrochemical Studies using Hydrodynamic Electrodes

Hydrodynamic electrodes can provide known, and reproducible mass transfer conditions and the performance of stationary electrodes cannot be compared with that of hydrodynamic systems [22]. The most popular devices under ambient conditions are the rotating disc electrode (RDE) and ring-disc electrodes (RRDE) [11, 23, 24], and for that reason the RDE will be described first.

#### 1.3.1 Rotating Disc Electrode System (HT-RDE)

The RDE has been used to investigate the mechanism of numerous electrochemical reactions under ambient conditions [22, 25]. The electrode is uniformly accessible, and the analysis of the experimental results is greatly simplified because of that. The electrode consists of a disc embedded in an electrical insulator (PEEK, PTFE, or epoxy). The hydrodynamic pattern (Figure 1-2) is achieved by rotating the electrode at a constant frequency in the solution. As a result of the rotation, the solution is pumped towards the electrode surface and then thrown outwards.

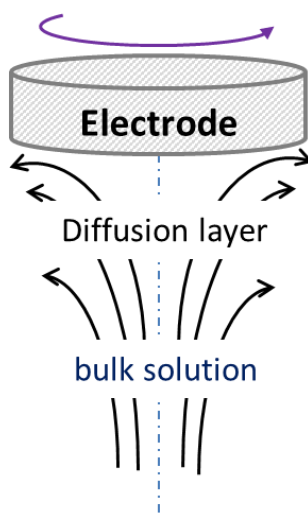


Figure 1-2: Schematic diagram of the RDE with the corresponding flow profile.

There are a few high T,p rotating disc electrode (HT-RDE) cells described in the literature [11, 12, 26]. The first system is due to Wojtowicz and Conway [26], who used the cell for studying the oxidation and reduction of ferrocyanide-ferricyanide, and the oxidation of hydrogen up to 90 °C. The temperature and pressure ranges were

limited, but it has the merit of being the first high temperature system ever attempted. Several years later, McBreen et al. [11] used an HT-RDE for studying the oxygen reduction reaction (ORR) up to 205°C and 7.6 bar, but there is no record that the system has been used for studying other systems.

Last year, a new HT-RDE concept was introduced by Fleige et al. [12]. The system consisted of a 100 mL glass beaker into a stainless steel autoclave, and stirring was provided by a magnetically coupled rotor (Figure 1-3). Despite the mobile parts, the absence of a high-pressure seal for the rotor is a huge advantage when comparing with the previous designs; however, the fabrication of the working electrode is still a problem, and the experiments were limited to 140°C and 100 bar.

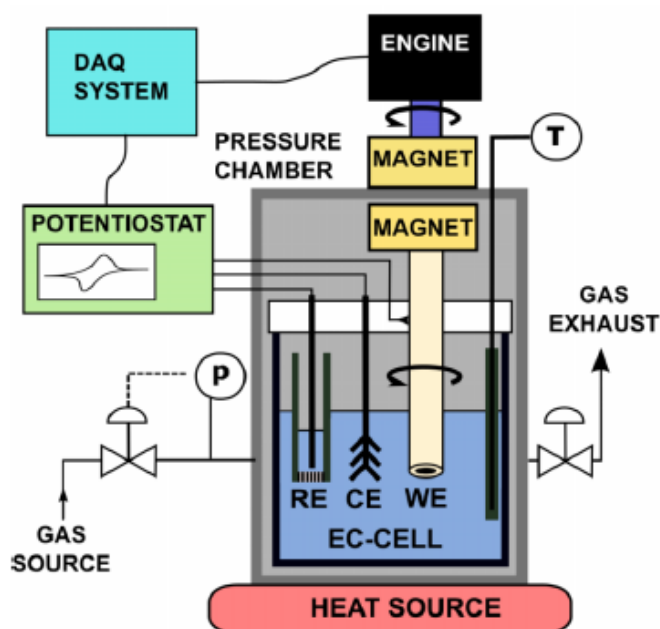


Figure 1-3: Schematic of a HT-RDE. Reproduced from [12], Copyright 2015, with permission from AIP.

Overall the system by Fleige and coworkers is interesting, but the set up is complicated and the residence time of the solutions at high temperature is long. It could be anticipated that problems like those found in static autoclaves experiments will be observed in this configuration. Also, it will be difficult to couple with other techniques.

### 1.3.2 Imping Jet Electrode Systems

The wall-jet electrode, WJE, and wall-tube electrode, WTE, are two interesting alternatives to the RDE; however only the wall-tube electrode has been considered for high temperature applications [8, 27]. In this configuration, the diameter of the jet is greater than the diameter of the electrode. The solution is pumped through a nozzle (under laminar flow conditions) and impinges on a surface containing the electrode (Figure 1-4).

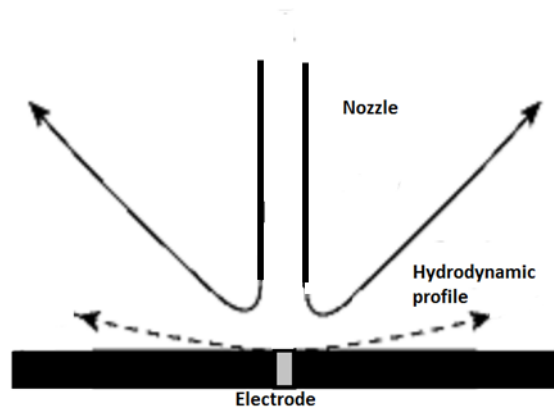


Figure 1-4: Wall-tube electrode (nozzle diameter  $\gg$  electrode diameter) [28].

Despite the different configuration of the working electrodes in the WTE and RDE cells, the convective-diffusion limiting current density expressions for the WTE (Eq.1-1) [29] and the RDE (Eq. 1-2) [22] are similar. T [29].

$$j_{lim} = \alpha \left( \frac{H}{d} \right)^{\beta} nF C_i \nu^{-1/6} D_i^{2/3} \omega^{1/2} \quad 1-1$$

$$j_{lim} = \alpha nF C_i \nu^{-1/6} D_i^{2/3} \omega^{1/2} \quad 1-2$$

Only the hydrodynamic constants ( $\alpha, \beta$ ) and  $\omega$  are different. For the RDE,  $\alpha = 0.62$ ,  $\beta = 0$ , and  $\omega$  is equal to the electrode rotation speed in Hz, while for the WTE,  $\alpha = 1.54$ ,  $\beta = -0.022$  and  $\omega = \frac{4V_f}{\pi d^3}$ , where  $V_f$  is the volume flow rate and  $d$  is the tube diameter [25]. The other parameters and variables are:  $F$  is the Faraday constant,  $\nu$  is the viscosity of solution,  $C_i$  and  $D_i$  are the molar concentration and the diffusion coefficient of the electroactive specie, respectively.



Trevani et al. developed a HT-WTE and studied simple one-electron redox reactions:  $\text{Fe}^{2+}/\text{Fe}^{3+}$  in  $\text{Na}_2\text{SO}_4/\text{KNO}_3$  up to 145 °C [8] and  $\text{I}/\text{I}_2$  up to ~ 215 °C at ~100 bar [27].

### 1.3.3 Annular-Duct and Channel Cell Electrodes

Similar to the impinging jet electrode systems, in these devices the electrode is fixed, and the hydrodynamic pattern is given by the flow of the solution and the shape and size of the duct or channel. Because of the cell geometry, the electrode is not uniformly accessible, and the mathematical treatment of the experimental data is harder than in the RDE [9, 20, 30, 31].

Balashov et al. [31] reported corrosion data for carbon steel up to 350 °C and 240 bar obtained with an annular duct flow cell. MacDonald [9] was able to calculate kinetic parameters (exchange current density and anodic transfer coefficients) for the oxidation of hydrogen on Pt in NaOH solutions up to 300 °C using a similar cell's geometry. The annular-duct cell configuration has some advantages in terms of electrode construction, and it is certainly an option to be considered, but the design is still complicated.

The number of studies involving channel flow cells is relatively large. However, most of the studies were limited to ambient conditions. Watanabe's group in Japan has expanded these studies to temperatures just above the boiling point of water (~ 90 - 110 °C) [32, 33]. These two-electrodes cells (similar to the RRDE system) were used to study the catalytic activity of metal and metal oxides. The cell design has changed very little over the years. It consists of two KEL-F blocks, the electrode used to support the catalysts nanoparticle films is usually gold and it is embedded on one of the KEL-F blocks. The channel is created by a thin PTFE sheet between the blocks that acts as a seal. The system operates under low pressure conditions (1 - 1.5 bar); the solution flask and the cell are both located in an oven to keep the temperature of the solution constant due to the low thermal conductivity of KEL-F. The dimensions of the channel are not reported in any of these studies.

Recently, attention has been focused on coupling UV-visible [34, 35], FTIR [36], Raman [37] and other spectroscopic methods with channel-type electrodes for the

simultaneous measurement of the absorption (scatter) spectra making this cell specially attractive for the investigation of the mechanisms of electrochemical reaction.

In summary, the CFC design offers some advantages over other hydrodynamic electrochemical techniques for high T,p research. Some of them are listed below:

- It does not involve mobile parts.
- The residence time of the solutions at high temperature is usually short (depends on the cell design). Thus, decomposition problems can be minimized.
- The geometry is compatible with spectroscopic methods.
- The system is compatible with two (or more) electrodes configuration.
- It is better than microelectrodes because the size of the electrode makes possible to carry out corrosion studies under hydrothermal conditions.

#### **1.4 Reference Electrodes for High Temperature Studies**

The main requirements for a high-temperature reference electrode were summarized by Macdonald [38]: (i) the potential should be constant and remain stable for the duration of the experiment and (ii) the electrode should be compatible with the solution under study. In many cases, an internal reference electrode at the same temperature and pressure of the working electrode can satisfy the requirement, but in other instances an external reference electrode at room temperature is more convenient despite a correction is required to account for the gradients in temperature and pressure [39].

One of the most widely used reference electrodes is the Ag/AgCl/KCl, despite the fact that some studies have shown the experimental potential values (versus Pt/H<sub>2</sub>/H<sup>+</sup>) deviates from the predicted thermodynamic potential at temperatures above 275 °C [38]. For alkaline media, the Hg/HgO electrode has been successfully used up to 200 °C; however at higher temperatures the volatility and toxicity of mercury can be a problem [1]. In the case of the hydrogen electrode (Pt/H<sub>2</sub>/H<sup>+</sup>), the fugacity of hydrogen is required to calculate the change of potential with temperature (Nernst equation), that it could be a problem at very high temperature due to the high vapour pressure of water [38].

It is clear that the choice of a suitable internal reference electrode is given by the system under study and the temperature and pressure ranges.

## 1.5 Aims and Objectives

As discussed, several aspects need to be taken into account when designing an electrochemical cell for hydrothermal studies, from the properties of the solvent as a function of temperature (density, viscosity, and dielectric constant) to the stability of the redox couple and the reference electrode used to measure the cell potential. The final goal of this thesis is the construction of an HT-CFC for spectroelectrochemical studies under hydrothermal conditions ( $> 150\text{ }^{\circ}\text{C}$  and 100 bar); this thesis constitutes the first step toward that goal. The research objectives are described below.

- Create a one-dimensional steady state mass transport model for a channel flow cell using COMSOL Multiphysics (COMSOL MP) that can be used to analyze different cell/electrode configurations.
- Design and construct a room temperature cell that it could be scaled up to operate under high T,p conditions. Use room temperature electrochemical data for a single one electrode reaction, the oxidation of ferrocyanide in KCl, to verify the accuracy of the numerical model.
- Use UV-visible spectroscopy to investigate the thermal stability of the  $\text{H}_2\text{Q}$  and BQ to evaluate if it is a good candidate for the evaluation of the HT-CFC at high temperature.

## 1.6 Thesis Outline

The work presented in this thesis is organised into five chapters:

- Chapter 1 is an overview of the field of high T,p electrochemistry and hydrothermal research. The chapter also provides a summary of the research objectives and goals.
- Chapter 2 is primarily oriented to provide the relevant background information on mass transport phenomena under hydrodynamic conditions and the derivation of the Nernst-Planck equation for a channel cell. An introduction to COMSOL MP, and

the numerical methods used for describing the experimental results is also provided in this chapter.

- Chapter 3 is devoted to summarize the experimental results obtained with the room temperature channel cell and the validation of the one-dimensional numerical model. Conclusions and recommendation for the construction of a high T,p cell are also provided.
- Chapter 4 is dedicated to describing the method used for studying the thermal stability of H<sub>2</sub>Q and BQ along with spectroscopic data up to 250 °C and 100 bar. The results are compared with bibliographic data, and the viability of using this system for validation of a future HT-CFC is addressed.
- Chapter 5 is a summary of the thesis main conclusions and future work.

## Chapter 2: Fundamental Concepts and Terminology

### 2.1 Electron Transfer and Mass Transport in Solution

The faradaic current associated with a particular redox reaction is the result of all the processes involved in the mechanism that it could be very complex or relatively simple as that shown in Figure 2-1. In this case, there are only three main processes involved: (i) mass transport of the electroactive species (A) to the electrode surface, (ii) the electron transfer process ( $A + e \rightarrow B$ ), and (iii) mass transport of the reaction product (B) back to the bulk solution. The reverse process can also take place by reversing the applied potential if the reaction is reversible or quasi-reversible [22, 28]. The current (or electrode reaction rate) is governed by the electron transfer and mass transfer of the electroactive species.

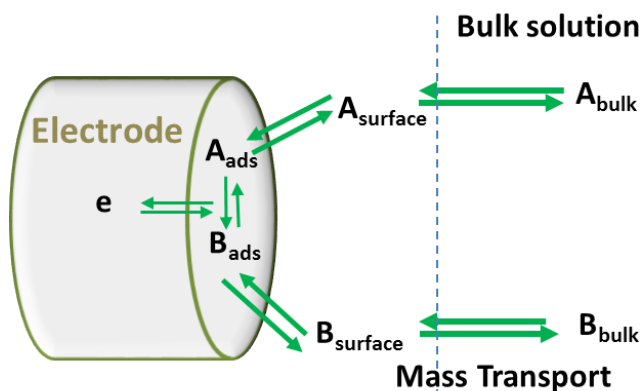


Figure 2-1: A schematic representation of a simple electrochemical process.

Despite the apparent simplicity, there are three different mechanisms through which an electroactive species can reach the electrode surface: diffusion due to a gradient of concentration (or chemical potential), migration due to a gradient of electrical potential, and convection (natural or forced) due to the movement of an element of volume of solution. The equation that describes the flux ( $J_A$ ) of an electroactive species “A” due to these three contributions is given by the *Nernst-Planck* equation [22, 28]:

$$J_A = -D_A \nabla c_A + C_A v + \frac{z_A F}{RT} D_A C_A \nabla \phi \quad 2-1$$

where  $D_A$  ( $\text{cm}^2.\text{s}^{-1}$ ),  $C_A$  ( $\text{mol}.\text{cm}^{-3}$ ), and  $z_A$  are the diffusion coefficient, the concentration, and the charge of the electroactive species, respectively.  $R$ ,  $F$ , and  $T$  are the gas constant, Faraday constant and absolute temperature, and  $v$  and  $\phi$  are the flow velocity and the electrical potential, respectively.  $\nabla$  is the differentiation operator in 3-D space that it can be greatly simplified by using Cartesians, cylindrical or spherical coordinates based on the geometry of the problem.

In the presence of a large excess of a supporting electrolyte, the third term due to migration is also negligible, and Eq. 2-1 reduces to the classical diffusion-convection equation:

$$J_A = -D_A \nabla c_A + C_A v \quad 2-2$$

where the first term is given by the Fick's law (diffusion) and the second term by the hydrodynamic conditions. Because the diffusion and convection contributions in the case of a channel flow cell are better described using Cartesians coordinates, only this case will be discussed in the following sections.

## 2.2 Diffusion Current: Fick's Second Law

To describe the change in concentration with time, as required in most of the problems related with electrochemistry, Fick's second law is needed:

$$\frac{\partial c_A}{\partial t} = -\nabla J_A = -\frac{\partial J_A}{\partial x} - \frac{\partial J_A}{\partial y} - \frac{\partial J_A}{\partial z} = D_{A,x} \frac{\partial^2 c_A}{\partial x^2} + D_{A,y} \frac{\partial^2 c_A}{\partial y^2} + D_{A,z} \frac{\partial^2 c_A}{\partial z^2} \quad 2-3$$

For normal diffusion (y direction), the contributions to mass transfer due to diffusion in the x (flow direction) and z directions can be assumed negligible (Figure 2-2), and the second Fick's law reduces to only one term:

$$J_A = -\frac{\partial c_{A,y}}{\partial t} = -D_{A,y} \frac{\partial^2 c_A}{\partial y^2} \quad 2-4$$

Eq. 2-4 can be used to get an expression for the change in concentration with the distance to the electrode surface and time. It can be then used to calculate the

concentration gradient at the electrode surface,  $\left(\frac{\partial C}{\partial y}\right)_{y=0}$ , caused by an applied potential and the diffusional current associated to that concentration gradient (Figure 2-2).

$$i = n F A D_A \left(\frac{\partial C_A}{\partial y}\right)_{y=0} \quad 2-5$$

In this equation, the diffusion coefficient was assume constant and independent of the distance to the electrode surface because the changes in solution composition in electrochemical studies is usually small due to the presence of a supporting electrolyte [22].

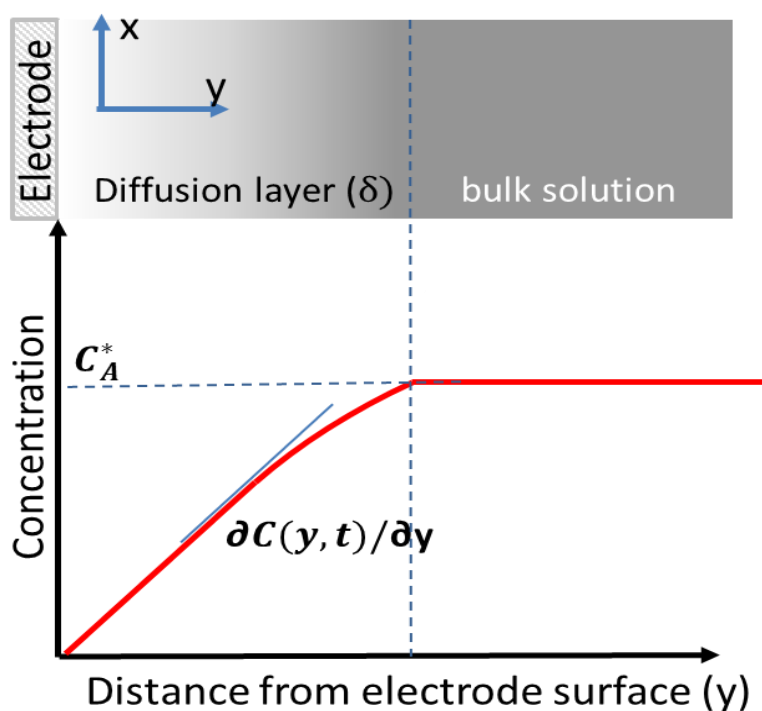


Figure 2-2: Concentration profile and diffusion layer approximation (dashed lines).  $x=0$  corresponds to the electrode surface, and  $\delta_0$  is the diffusion layer thickness.

## 2.3 Theoretical Treatment of Convective Systems

### 2.3.1 Channel Flow Cell: Diffusion-Convection Equation

Hydrodynamic methods use convection to enhance the rate of mass transport to the electrode and have several advantages over techniques that operate in stagnant

solutions. There are two main reasons why convection is introduced. First, the use of convection usually results in higher currents and sensitivity; second, it is possible to control the mass transport to the electrode surface by changing the fluid velocity [22, 25].

As outlined in a previous section, the diffusion-convection equation for a simple redox process,  $A + ne \rightarrow B$ , is given by Eq. 2-2. In the case of a channel electrode, the electrode is embedded in one of the walls of a rectangular duct through which the electrolyte flows. In practice, the geometry of the cell and the experimental conditions (laminar flow) are selected to simplify the problem and reduce the 3D fluid velocity profile (Eq. 2-6) to a one-dimensional problem.

$$v(x, y, z) = i v_x + j v_y + k v_z \quad 2-6$$

In the case of channel flow cell under laminar flow conditions, this goal can be achieved by making the two following assumptions [17, 40, 41]:

- The solution parabolic flow in the direction of the flow (x) can be approximated to a linear function of the distance to the electrode surface (y) (Levich's approximation). This assumption is only valid if the diffusion layer,  $\delta$ , is small compared with the height of the channel,  $2h$ .

$$v_x = v_0 \left(1 - \frac{(y-h)^2}{h^2}\right) \quad 2-7$$

where  $v_0$  represents the linear velocity of the solution at the centre of the channel and can be calculated from the volume flow rate through the equation:

$$v_f = v_0 \int_0^d \int_0^{2h} \left(\frac{h^2 - (y-h)^2}{h^2}\right) dy dz = \frac{4}{3} v_0 h d \quad 2-8$$

- The mass transfer due to convection in the direction of the flow (x) is much greater than the contribution due to diffusion in the x and z directions.

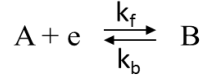
$$v_x \frac{\partial C_A}{\partial x} \gg D_A \left( \frac{\partial^2 C_A}{\partial x^2} + \frac{\partial^2 C_A}{\partial z^2} \right) \quad 2-9$$



The diffusion-convection equation for a channel cell after these approximations becomes:

$$\frac{\partial c_A}{\partial t} = D_A \frac{\partial^2 c_A}{\partial y^2} - v_x \frac{\partial c_A}{\partial x} \quad 2-10$$

On the other hand, for following reaction;



The current density for a simple electron transfer reaction is given by the Butler-Volmer equation:

$$i = nFA k_0 \left( c_A(0, t) \exp\left(\frac{(n-\alpha_c)F\eta}{RT}\right) - c_B(0, t) \exp\left(\frac{-\alpha_c F\eta}{RT}\right) \right) \quad 2-11$$

In which  $k_0$  is the *heterogeneous rate constant* of the reaction,  $\alpha_c$  is the *cathodic transfer coefficient*, and  $\eta$  is the overpotential at the working electrode which equals to  $E - E^0$ .

The total current recorded at the electrode can be extracted by integrating the local current density across the electrode. It is not sufficient to simply multiply by the area of the electrode, because the current density may be non-uniform. An Integral Component Coupling is used to define an electrode current variable according to Eq. 2-5;

$$I = -FD_A w \int_0^{x_e} \left( \frac{\partial c_A}{\partial y} \right)_{y=0} dx \quad 2-12$$

Then the analytical solution for the limiting current in a channel cell, the Levich equation is given by:

$$I_{lim} = 0.925 n F C_A w x_e^{2/3} D^{2/3} \left( \frac{v_f}{h^2 d} \right)^{1/3} \quad 2-13$$

where  $n$  is the number of electrons involved in the electron reaction,  $C_A$ ,  $D_A$ ,  $V_f$ ,  $h$ ,  $w$ ,  $x_e$ , and  $d$  were just defined.

The approximations made to reach Eq. 2-13 are not always valid, since they are strongly dependent on the electrode and channel dimensions and the volume flow rate,

then numerical simulation is required to solve the *Navier-Stokes* and *Nernst-Planck* equations and get information about the mechanism of reaction and limiting currents from the experimental results [22, 25].

### 2.3.2 Determination of Velocity Profile

A brief discussion of some of the concepts, terms, and hydrodynamic equations is included here to provide the minimum background information required for understanding the numerical simulation approach.

For an incompressible fluid (i.e. a fluid whose density is constant in time and space), the velocity profile is obtained by solution of the *continuity* (Eq. 2.14), and *Navier-Stokes* equations (Eq. 2.15), with the appropriate boundary conditions.

The *continuity* equation is a statement of incompressibility (density is constant in time and space) [22];

$$\nabla \cdot v = 0 \quad 2-14$$

where the *Navier-Stokes* equation (represents Newton's first law;  $F = m a$ );

$$\rho \frac{\partial v}{\partial t} = -\nabla P + \mu \nabla^2 v + f \quad 2-15$$

where  $v$ ,  $\rho$ , and  $\mu$  are the velocity, density and dynamic viscosity of the fluid, respectively,  $P$  is the fluid pressure,  $f$  represents the effect of natural convection arising from the buildup of density gradient in the solution, and the other parameters and symbols were defined in previous sections. The first, second and third terms on the right represent forced convection, frictional forces, and natural convection, respectively [22]. For an incompressible fluid,  $f=0$  and the equation only involves the two first terms on the right.

The *Navier-Stokes* equations represent the conservation of momentum while the *continuity* equation represents the conservation of mass. These equations are the heart of fluid flow modeling. The solution of the hydrodynamic equations requires writing the equations in the appropriate coordinate system, specifying the boundary conditions and usually, solving the problem numerically. In electrochemical problems, only the

steady-state velocity profile is of interest; therefore *Navier-Stokes* equation is solved for  $dv/dt=0$ .

Figure 2-3 show the flow behaviour through a pipe under turbulent and laminar conditions (smooth channel walls). For an ideal (smooth and uniform channel), the transition between laminar and turbulent flow can be predicted using the Reynolds number,  $Re$ , which relates the linear flow rate,  $v_o$  (cm/s), a characteristic length,  $l$  (cm) in the system and the viscosity of the solution,  $\nu$ , at a particular temperature and pressure [22];

$$Re = \frac{v_o l}{\nu} \quad 2-16$$

Under laminar flow conditions, the fluid dynamics within the cell can be predicted by the *Navier-Stokes* and *continuity* [25].

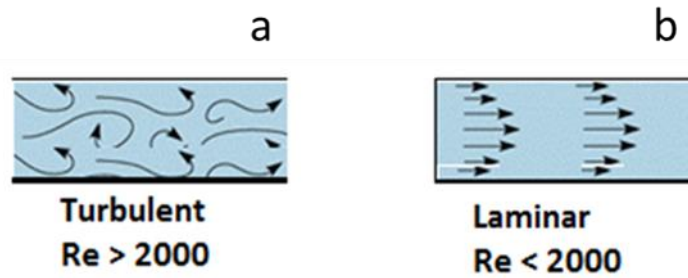


Figure 2-3: Possible flow pattern in a pipe or channel: (a) Turbulent flow, (b) Laminar flow.

## 2.4 Numerical Simulation

Mathematical modeling is a useful tool for design and validation of experimental data from a system. Less time is involved in performing a computational analysis than in developing, fabricating, and subsequently testing systems with various geometries and parameters. However, the simulation results are only confirmed once experimental results are available to verify the findings are correct. Computational simulations can be performed with manually written code or commercial software packages, but because of the complexity of many electrochemical processes, several commercial computational packages have become popular within the electrochemical community. Some examples of commercially available software packages are: COMSOL

Multiphysics (formally Femlab; COMSOL, Inc.), Fluent (ANSYS, Inc.), CFD-ACE + (CFD Research Corp.) and Coventor (Coventor, Inc.) [42].

#### **2.4.1 Finite Element Analysis**

The finite element method is a computational scheme used to solve field problems in engineering and science. It has been used to solve a number of different problems: stress analysis, fluid mechanics, heat transfer, diffusion, vibrations, electrical and magnetic fields, etc [42-45]. The fundamental concept in this approach is to divide the body under study into a finite number of pieces (subdomains) called elements, and use an algebraic system of equations that can approximate the continuous solution to the actual problem. The elements size and shape and the approximating scheme can be varied to suit the problem under investigation, for this reason, the method can be used to accurately describe problems of complex geometry and conditions such those find in electrochemistry.

#### **2.4.2 Simulations Using COMSOL MP**

COMSOL MP has been used for modelling different kind of electrochemical systems, from polymer electrolyte fuel cells [46] to channel cell electrodes [34, 42]. An analysis of the publications during the last four years shows that most of studies were related to analytical electrochemistry involving one or more of the following problems: non-standard or complex geometry [43]; hydrodynamic electrochemistry [42, 44, 47]; or, multiple or complex reaction chemistry, whether several hetero- or homogeneous reactions are involved [30, 44]. The general procedure used in this thesis is described in the flow diagram in Figure 2-4.

The software uses the finite element method to solve a set of partial differential equations (PDEs). The finite elements are assembled by creating a “mesh”, a pattern made of identical shapes, on the geometry, for example, triangles in 2D or tetrahedral in 3D. To minimise the numerical error, which happens in any discrete numerical method, the use of an appropriate mesh is essential. In the case of the channel cell, the model definition includes:

- The geometry and dimensions of the channel ( $l$ ,  $d$ ,  $2h$ )

- The flow conditions (laminar or turbulent)
- The physical properties of the system (temperature, pressure, concentration, density, viscosity, diffusion coefficients, etc)
- Meshing and a set of boundary conditions.

The *Navier-Stokes* equation is solved first with an initial set of conditions to accelerate convergence (Computational Fluid Dynamic module). The results are used to solve the *Nernst-Planck* equation (Electroanalysis module), and the procedure is repeated until convergence is obtained based on a predefined relative error in the current density ( $< 0.01$ ). To simplify the mathematical treatment, the calculations are done assuming the presence of an excess of supporting electrolyte to eliminate the migration term in the *Nernst-Planck* equation. The current–voltage electrode response under a given set of experimental conditions is obtained using the *Butler-Volmer* equation (Eq. 2-11) since the current density is a function of the electrode potential and the concentrations of the reactants at the electrode surface.

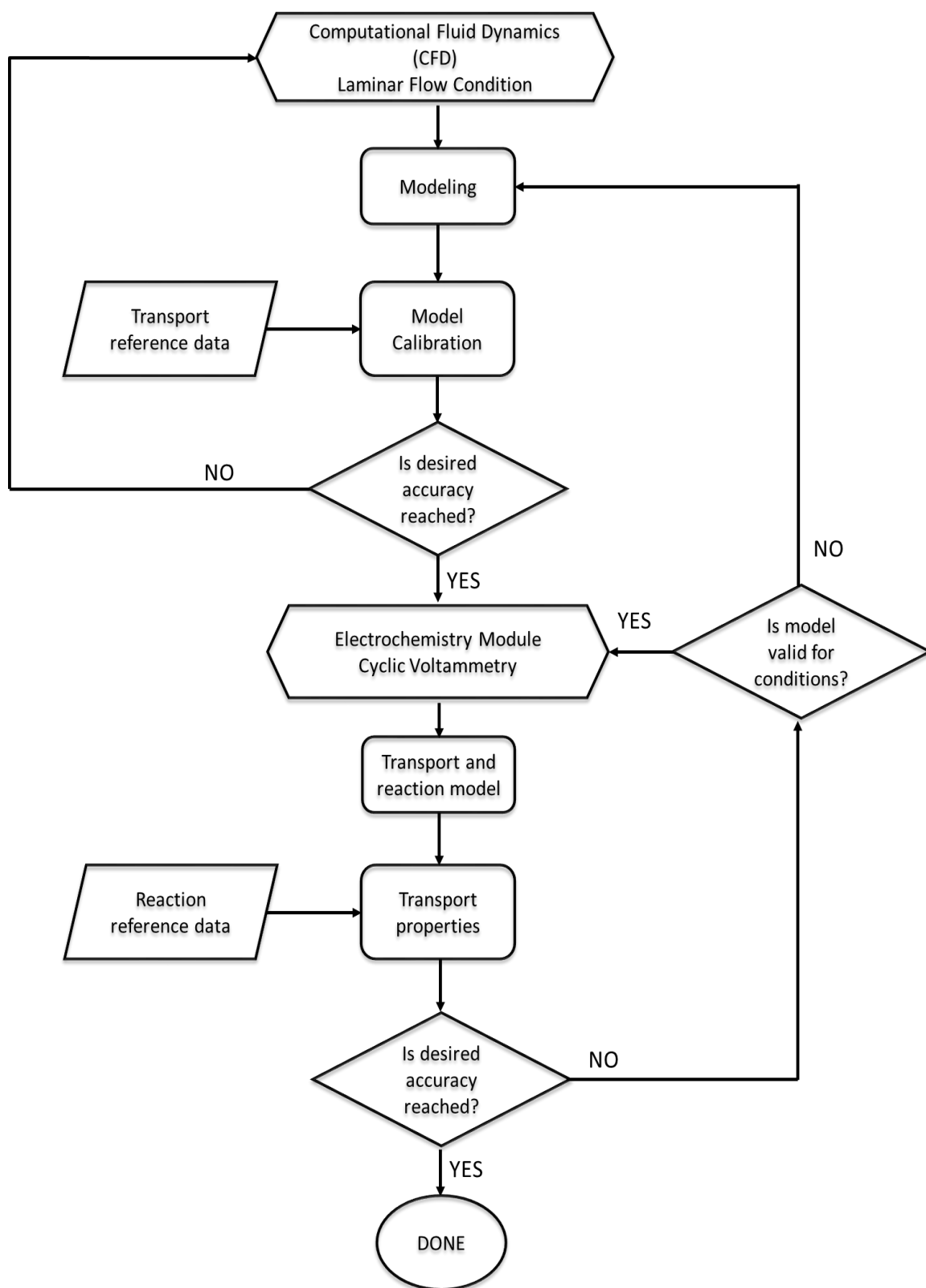


Figure 2-4: Finite element simulation method used in COMSOL MP to predict linear sweep voltammetry results in a channel flow cell.

## Chapter 3: HT-CFC Design Optimization using a Numerical Simulation Method

### 3.1 Introduction

Channel flow cells have been widely used for both fundamental and applied research in the field of electrochemistry [15, 32, 33, 40, 41]. There are several reasons for that, the design is simple, allows the use of more than one electrode, and it is compatible with spectroscopic methods. The cell itself consist of two-part or three-part components. In the latter case (which is the most common), the parts are: (i) an electrode either embedded (or glued) in the bottom part of the channel; (ii) a spacer, the thickness of which defines (approximately) the channel height, and (iii) a top block, which typically includes the flow inlet and outlet pipes. The cell is usually held together by the use of nuts and bolts [34]. The geometry of the channel (Figure 3-1) plays a significant role in the hydrodynamic properties. Typical CFC dimensions and volume flow rates reported in the bibliography are summarized in Table 3-1.

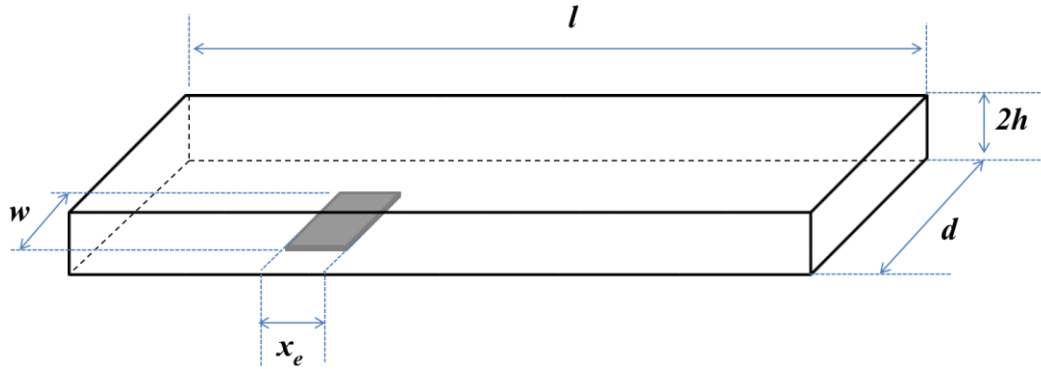


Figure 3-1: Channel Flow Cell (CFC) dimensions.

Table 3-1: Common CFC configuration in the bibliography.

Channel dimensions		Electrode dimension		Flow rate $\text{cm}^3 \cdot \text{min}^{-1}$	References
Width (d/mm)	Height (2h/mm)	Length (w/mm)	Width (x <sub>e</sub> /mm)		
6	0.36	4	4	2.5 to 16.5	[15]
---	0.5	6	5	80	[48]
2	0.116	2	0.012	2.5 to 17	[49]
6	1	4	4	0.32 to 1	[35]
3	0.250	3	0.68	0.1 to 64	[34]
3	0.192	2	0.20	0.1 to 25	
2	0.058	1.2	0.001	9 to 72	[50]
			0.005		
			0.010		
30	1	10	25	3 to 80	[51]

Out of all the flow cell designs reviewed, the smaller cells are the most convenient for high temperature applications, because it will reduce the residence time of the solutions at high temperature, and even more important higher mass transfer rates can be achieved at relatively low flow rates, an extremely important aspect considering the solution needs to reach the target temperature before entering the channel.

## 3.2 Experimental Section

### 3.2.1 Chemicals and Materials

The solutions were prepared using deionized water with a resistivity of 18  $\text{M}\Omega \cdot \text{cm}$ . Potassium ferrocyanide, ( $\text{K}_4\text{Fe}(\text{CN})_6 \cdot 3\text{H}_2\text{O}$ , 98.5-102.0%, ACS reagent), potassium ferricyanide ( $\text{K}_3\text{Fe}(\text{CN})_6$ ,  $\geq 99.0\%$ , ACS reagent) and KCl (99 -100.5 %, ACS reagent) were all purchased from Sigma-Aldrich and used as received. The solutions were prepared before the experiments and kept under a nitrogen atmosphere (99.999% NI5.00H-T, Praxair Canada Inc) before and during the electrochemical runs.



### 3.2.2 Electrochemical Experiments

A three-electrode cell was used for the electrochemical experiments at room temperature. A Pt band working electrode (WE,  $0.4 \text{ cm}^2$ ), a Pt counter electrode (CE) with an area greater than that of the WE, and one of these two different reference electrodes (RE): a commercial Ag/AgCl/0.1 M KCl from Pine Research Instruments and a pseudo RE consisting of a Pt wire immersed in an  $\sim$  equimolar ( $10^{-3} \text{ M}$ ) ferrocyanide/ferricyanide solution in 0.1 M KCl. The electrochemical experiments were performed using a Gamry - Reference 600 Potentiostat/ Galvanostat/ ZRA. The linear sweep voltammograms were recorded under nitrogen at a sweep rate of  $20 \text{ mV.s}^{-1}$ . The electrode was polished between experiments using wetted microcloth polishing pads using  $0.3 \mu\text{m}$  flowed by  $0.05 \mu\text{m}$  alumina micropolish (CH Instruments, Inc.). A similar approach was adapted when using the RDE system (Pine Research Instruments).

### 3.2.3 CFC: Room Temperature Prototype

The room temperature prototype was constructed using Plexiglass because it was easier for machining than titanium; it is a material that was used in other studies [51, 52], and it is easy to trace any perturbations caused by the formation of bubbles. However, other materials such as Kel-F [33], or quartz [14] for spectroelectrochemical applications could be also used.

The CFC prototype is shown in Figure 3-2. The Pt WE ( $x_e = 1 \text{ mm}$  and  $w = 4 \text{ mm}$ ) is embedded in a flat Plexiglass plate to allow changing the electrode size/composition and polishing the electrode surface between experiments. The cell is completed by other two Plexiglass pieces, one of them houses the solution inlet and outlet ports for two  $1/16''$  PEEK connector and the channel ( $2h = 1 \text{ mm}$  (height),  $d = 4 \text{ mm}$  (width) and  $l = 4 \text{ cm}$  (length)). The reference and counter electrode were located at the input and output of the channel, respectively.

One of the major problems when making the working electrode was to get a well-defined area, flat surface without any crevices, and a good electrical connection. In the original configuration, the working electrode was a small  $2 \text{ mm} \times 2 \text{ mm} \times 0.1 \text{ mm}$  Pt plate similar to that in references[15]. Unfortunately, this configuration showed to be problematic in our case, the epoxy silver used to make the electrical connection was in many instances exposed to the solution resulting in different kind of undesirable

artefacts on the LSVs or resulted in a poor electrical connection. Soldering the Pt electrode to a Pt wire was also intended, but the surface of the Pt electrode was not perfectly flat, and the presence of small “bumps” on the surface could induce turbulences in the flow and the assumption of laminar flow for Reynolds numbers below 2000 would not be valid. For the reasons exposed, a band electrode (1 mm  $\times$  4 mm) was used for the runs. The new configuration has the advantage that it can be easily implemented in a high T,p cell.

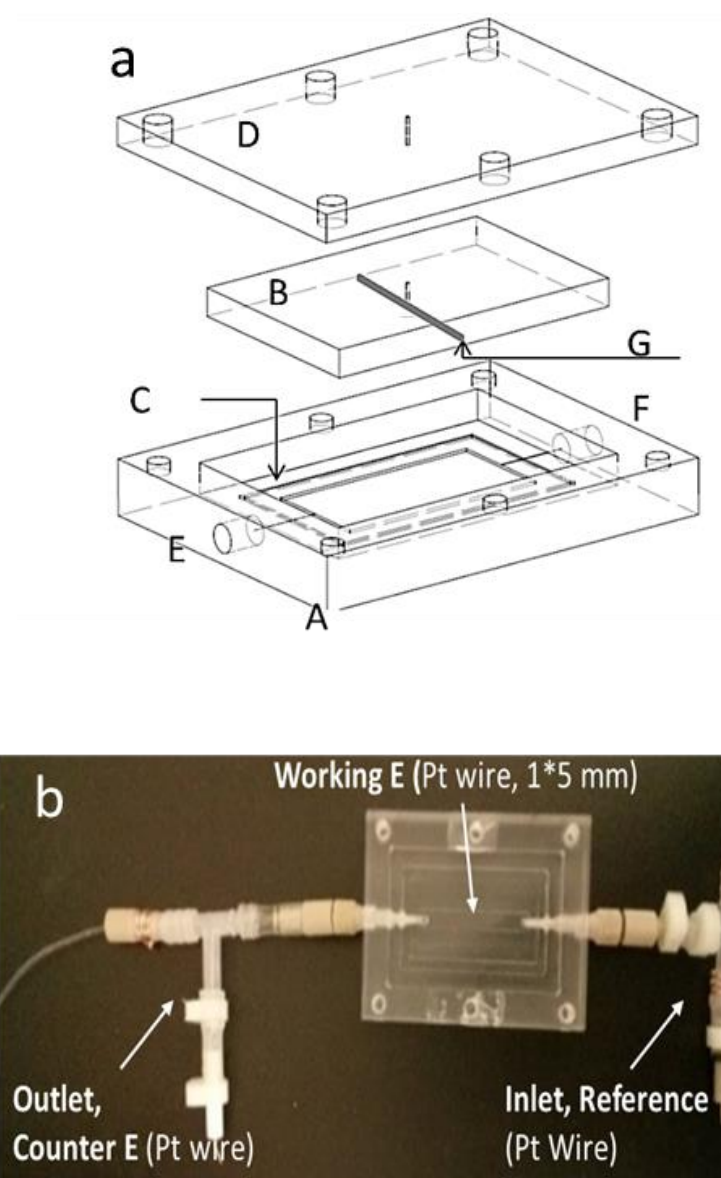


Figure 3-2: (a) Schematic diagram of the room temperature CFC: (A) cell body; (B) electrode support; (C) o’ring; (D) bolted end-cap; (E) inlet; (F) outlet and (G) Pt working electrode; (b) picture of the cell after assembling.

### 3.3 Numerical simulations

COMSOL MP was used to simulate the experimental results obtained with the room temperature prototype and investigate possible alternative designs for the construction of a high T,p channel cell.

#### 3.3.1 COMSOL MP Model

A three-dimensional rectangular channel was selected based on the dimensions of the room temperature prototype and the band electrode ( $1\text{ mm} \times 4\text{ mm}$ ) was chosen to reproduce the experimental conditions (Figure 3-3).

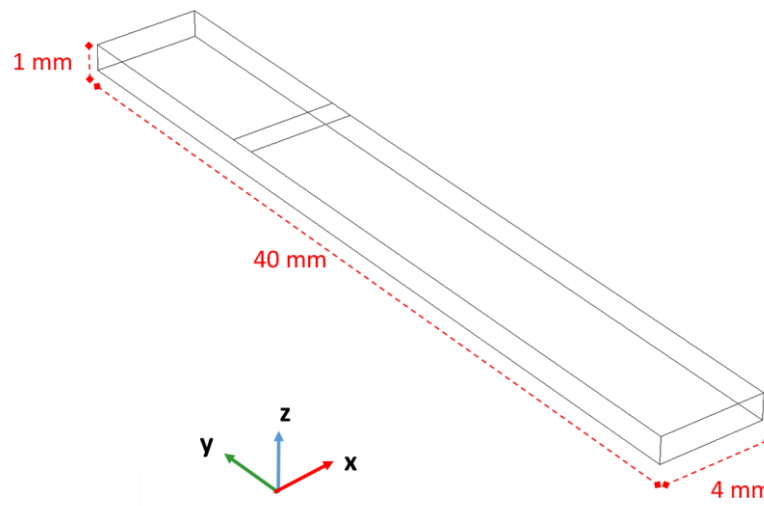


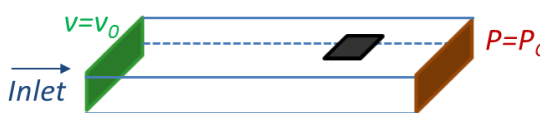
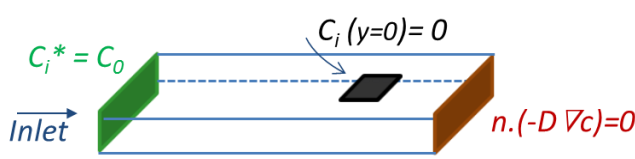
Figure 3-3: Physical descriptions of the channel and electrode ( $2h=1\text{ mm}$ ,  $d=4\text{ mm}$ ,  $l=40\text{ mm}$ ).

In the model set-up the following conditions were used: i) steady-state operating conditions, ii) single phase system, iii) Newtonian fluid (constant density and viscosity at a given temperature and pressure), iv) physical properties of water (viscosity and density) valid for dilute solutions, and v) one electron redox process without coupled homogeneous reactions.

The boundary conditions used to solve the *Navier-Stokes* and *continuity* equations, the *Nernst-Planck* diffusion-convection terms, and the *Butler-Volmer* equation are summarized in Table 3-2. For the *Navier-Stokes* equation, the fluid velocity ( $v = V_f$ ) is defined first, and the velocity at the walls is set equal to zero,  $v=0$ ; which referred to as the no-slip condition.

Moreover, in COMSOL the absolute pressure,  $P_a$ , defined as  $P_a = p + p_{ref}$  where  $p$  and  $p_{ref}$  are the pressure of the system and the reference pressure, respectively. The pressure of the system is calculated by COMSOL based on the flow rate and the channel dimensions, and by default is zero at the outlet. On the other hand, the reference pressure all around the system is typically 1 [atm] at sea level, but it can take any other value depending on the experimental conditions. After determining the velocity profile ( $v_x$ ,  $v_y$ ,  $v_z$ ) at a particular  $V_f$  value, the solution is used to solve the steady-state convection-diffusion equation. The initial bulk concentration of an oxidized species (for a reduction reaction) is assumed at the inlet  $C_i^* = C_o$ . The convective flux is set at the outlet [n.  $(-D\nabla c) = 0$ ], and the walls are defined as to be insulating [n.  $(-D\nabla c + cv) = 0$ ]. Also, to simulate limiting current conditions, the concentration of the electroactive species at the electrode surface was set equal to zero  $C_i(y=0)=0$ . Since we are applying steady state condition, initial values at time zero must be also defined.

Table 3-2: Navier-Stokes and convection/diffusion transport equations and boundary conditions for numerical modeling.

CFD Module	
<i>Navier-Stokes and Continuity equations</i>	$\rho \frac{\partial v}{\partial t} = \eta \nabla^2 v - \nabla P$ $\nabla \cdot v = 0$
<i>Boundary condition</i>	 <p>No slip condition on walls (except the inlet and outlet)</p>
Electroanalysis Module	
<i>Nernst-Plank equation (Conv. +Diff)</i>	$\frac{\partial c_A}{\partial t} = D_A \nabla^2 c_A - \nabla c_A v$
<i>Butler-Volmer equation</i>	$i = nFk_0 \left( c_A \exp \left( \frac{(n - a_c)F\eta}{RT} \right) - c_B \exp \left( \frac{-a_c F\eta}{RT} \right) \right)$
<i>Boundary condition</i>	

### 3.4 Results and Discussion

#### 3.4.1 Electrochemical Studies-Cell Evaluation

The room temperature cell performance was evaluated by studying the oxidation of  $\text{Fe}(\text{CN})_6^{4-}$ , a one electron redox reaction for which the diffusion coefficients of both  $\text{Fe}(\text{CN})_6^{4-}$  and  $\text{Fe}(\text{CN})_6^{3-}$  are well known in different media and temperature/pressure conditions. Nevertheless, to avoid discrepancies when comparing with the CFC results, the diffusion coefficient of  $\text{Fe}(\text{CN})_6^{4-}$  in the actual solution was also determined using an RDE system. Figure 3-4 shows typical LSVs for the oxidation of  $\text{Fe}(\text{CN})_6^{4-}$  obtained using a Pt RDE ( $0.196 \text{ cm}^2$ ) electrode at a scan rate of  $20 \text{ mV/s}$ , along with the Levich's plot,  $i_{\text{lim}}$  at  $0.4 \text{ V}$  (plateau region) vs  $\omega^{1/2}$ . The diffusion coefficient for  $\text{Fe}(\text{CN})_6^{4-}$  in KCl,  $7.0 \times 10^{-6} \text{ cm}^2/\text{s}$ , obtained from the Figure 3-4 and Eq. 1-2, is in good agreement with other reported values in the bibliography (Table 3-3).

Table 3-3: Diffusion coefficient,  $D$ , for  $\text{Fe}(\text{CN})_6^{4-}$  as reported by other authors at  $25^\circ\text{C}$ .

$D \times 10^6 (\text{cm}^2.\text{s}^{-1})$	Supporting electrolyte	References
$6.3 \pm 0.2$	0.1 M KCl	[14]
$6.58 \pm 0.37$	0.1 M KCl	[25]
7.0	0.1 M KCl	[23]
$6.0 \pm 0.5$	0.1 M KCl	[53]
$5.7 \pm 0.5$	0.2 M $\text{KNO}_3$	[51]
7.0	0.1 M KCl	This work

Once the diffusion coefficient was determined, linear sweep voltammetry experiments were carried out using the CFC to estimate the hydrodynamic constant for the cell. Figure 3-5 (a) summarizes the LSVs for the oxidation and reduction of  $\text{Fe}(\text{CN})_6^{4-}$  ( $0.95 \text{ mM}$ ) and  $\text{Fe}(\text{CN})_6^{3-}$  ( $1.27 \text{ mM}$ ) in  $0.1 \text{ M KCl}$  at flow rates equal to 6, 10, 14,  $18 \text{ cm}^3.\text{min}^{-1}$ . The LSVs show the characteristic pattern for a reversible couple, and a well-defined mass transport region (plateau) for all of the flow rates studied. Figure 3-5 (b) shows the limiting current data at  $0.3 \text{ V}$  (vs the Pt pseudo reference electrode) as a function of the cubic root of the solution volume flow rate ( $V_f$ )<sup>1/3</sup>. The hydrodynamic constant,  $\alpha$  can be obtained from the Levich's plot slope using Eq.3-1 and the  $D$  value reported in Table 3-3.

$$I_{lim} = \alpha FC w x_e^{2/3} D^{2/3} \left(\frac{1}{h^2 d}\right)^{1/3} V_f^{1/3} \quad 3-1$$

The experimental  $\alpha$  value for the band electrode was equal to 0.997, 7.8% greater than the hydrodynamic constant in Levich equation, 0.925 [22].

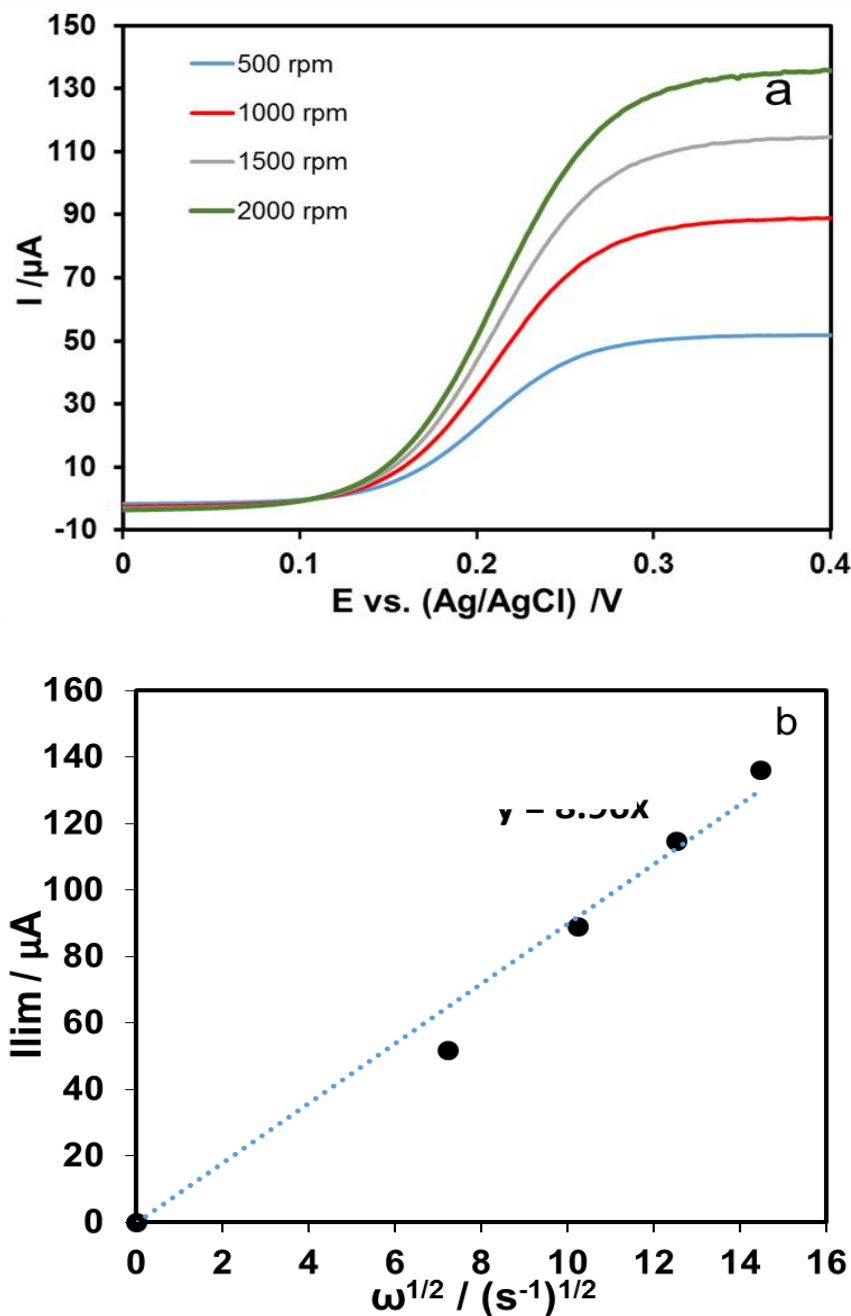


Figure 3-4: (a) Linear sweep voltammograms for the oxidation of 1.5 mM ferrocyanide in 0.1 M KCl obtained using a RDE at different rotation rates (scan rate: 20 mV.s<sup>-1</sup>), (b) Levich's plot for the same.

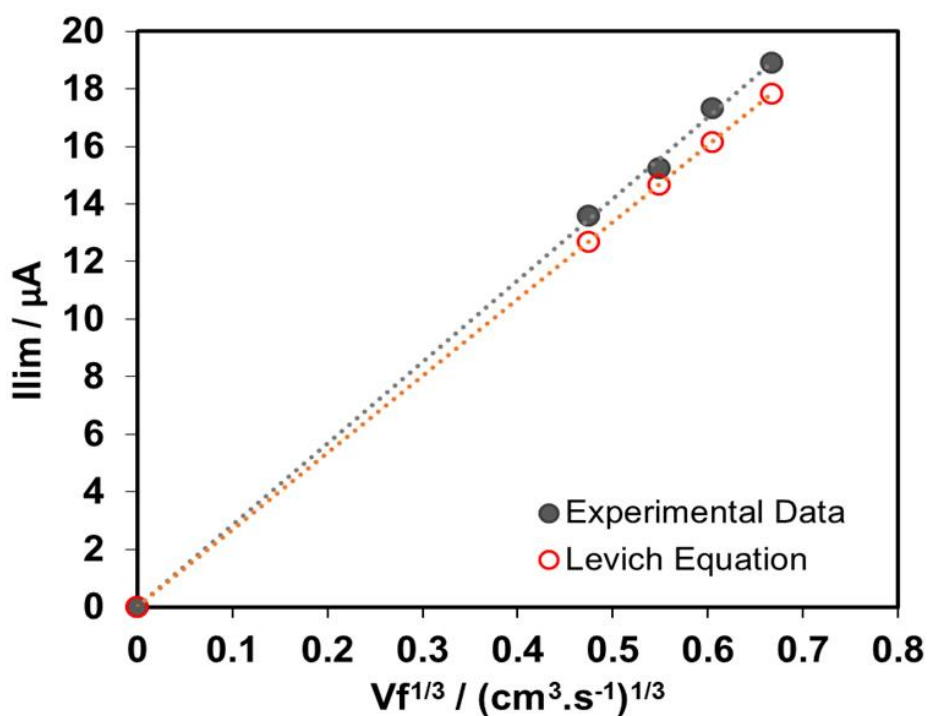
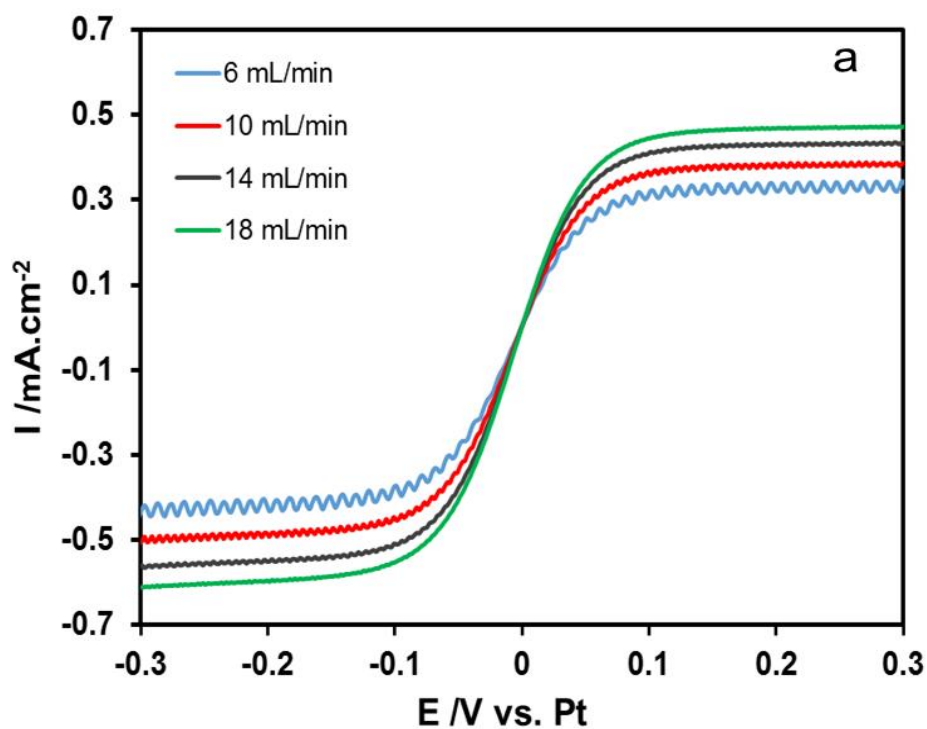


Figure 3-5: (a) Linear sweep voltammograms for the oxidation of 0.95 mM ferrocyanide and reduction of 1.27 mM ferricyanide in 0.2 M KCl in a CFC at different flow rates (scan rate: 20 mV.s<sup>-1</sup>), (b) Levich plot ( $i_L$  vs  $V_f^{1/3}$ ) for the oxidation of ferrocyanide.

In terms of diffusion layer thicknesses ( $\delta$ ), the volume flow rates in the experiments summarized in Figure 3-6 are equivalent to those in a RDE at rotation

frequencies between 1500 - 2000 rpm. These values were calculated with Eq. 3-2 and a D value equal to  $7 \times 10^{-6} \text{ cm}^2/\text{s}$  ;

$$\delta = 0.858 \left( \frac{hDx_e}{v_m} \right)^{1/3} \quad 3-2$$

where  $v_m$  is the mean solution velocity ( $\text{cm.s}^{-1}$ );

$$v_m = \frac{v_f}{2hd} \quad 3-3$$

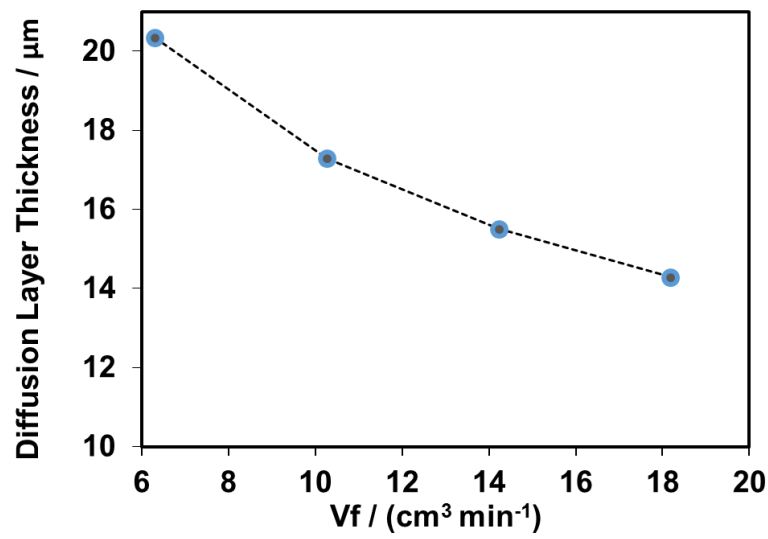


Figure 3-6: Diffusion layer thickness in a CFC vs. volume flow rate.

### 3.4.2 Evaluation of Numerical Simulation Results

The solution obtained for the diffusion-convection terms in the *Nernst-Planck* equation (Eq. 2-1) is based on a number of assumptions. As mentioned in Chapter 2, the solution could not be necessarily valid for all geometries (size of the channel, dimension of the electrode, and flow rate), for that reason and because of the need of reducing the volume flow rates in future cell designs, numerical simulation was used to analyze CFC experimental data [41, 44, 47]. COMSOL MP is the commercial package used for the numerical simulations; several aspects related with the numerical procedure used to reproduce electrochemical data were introduced in Chapter 2.



### 3.4.2.1 Current-Voltage Simulation results

Figure 3-7 illustrates typical current-voltage traces obtained using COMSOL MP at the flow rates used on the CFC experiments. The LSV curves show the expected sigmoidal pattern for kinetic and mass transport control at low and high over potentials, respectively [22]. The current starts to growth at  $\sim -0.1$  V that is the overpotential ( $E - E_{\text{ref}}$ ) that in this case was chose equal to 0 V. The half-wave potential is greater than that expected for a reversible reaction, but this is probably due to the kinetic constant used for the oxidation reaction. Since the use of COMSOL MP for simulating kinetic reaction data is out of the scope of this thesis, this is a problem that it will be analyzed in more detail in the future. The limiting current values in Figure 3-7 are independent of the reference electrode or the kinetic constant values used for the simulations, as long as a plateau is achieved. The limiting currents can be used to evaluate the diffusion-convection pattern in different cell configurations.

As mentioned, the selection of the “best” mesh has a big impact on the success of the modeling process, for this reaon, the effect of the mesh selection and size on the current-voltage simulation will be discussed first.

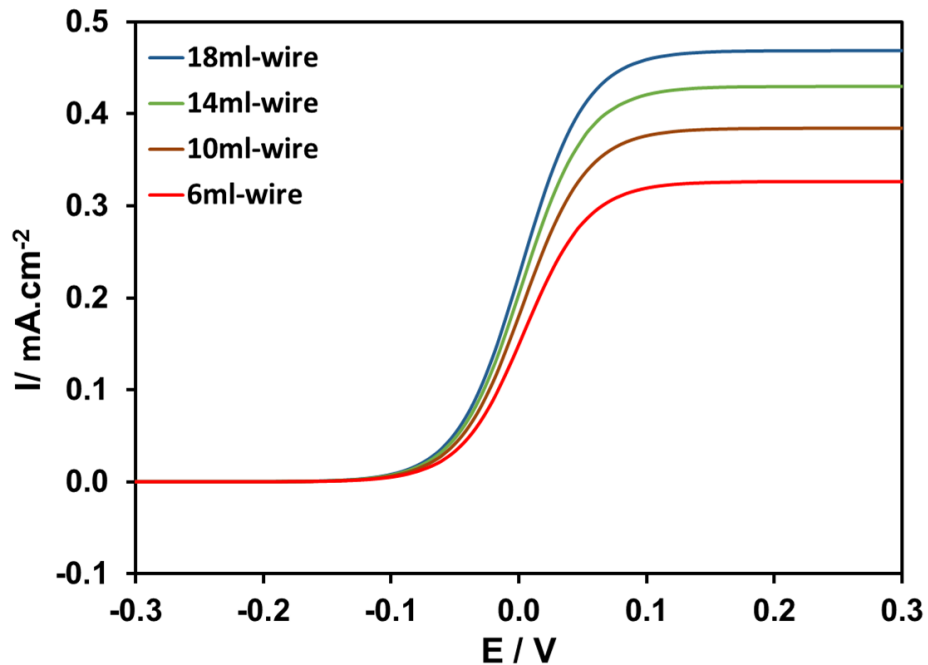


Figure 3-7: Limiting current density for the oxidation of 0.95 mM ferrocyanide for a band electrode ( $w=4\text{mm}$ ,  $x_e=1\text{mm}$ ,  $2h=1\text{mm}$ ) at  $V_f$  values of 6,10,14,18  $\text{cm}^3.\text{min}^{-1}$ .

### 3.4.2.2 Effect of Mesh Selection on the Limiting Current Values

COMSOL MP Software incorporated an automatic finite element meshing (FEM) technique, but the automatic mesh option is often inappropriate unless specific bounds are defined and areas of interest selected [43]. In other words, a system should be well meshed in all domains. The meshes used in this study to describe the channel and the electrode surface are shown in Figure 3-8 and Figure 3-9. It is worth noting that the higher is the number of elements in a mesh, the more accurate is the solution; however, the smaller the mesh, the longer is the computational time required to solve the equations. For simplicity, the parameters used for the numerical simulations are all summarized below, despite some of them were given in previous sections.

Table 3-4: Meshing properties selected for the simulation of room temperature prototype CFC.

Electrode length (xe)	0.1 cm
Electrode width (w)	0.4 cm
Channel height (2h)	0.1 cm
Channel width (d)	0.64 cm
Diffusion coefficient (D)	$7 \times 10^{-6} \text{ cm}^2 \cdot \text{s}^{-1}$
Bulk concentration ( $[A]_{\text{bulk}}$ )	$0.95 \times 10^{-6} \text{ mol} \cdot \text{cm}^{-3}$
<b>Meshing properties of electrode (Triangular)</b>	
Maximum element size	0.0025 cm
Minimum element size	0.0000524 cm
Number of boundary layers	20
Boundary layer stretching factor	1.2
<b>Meshing properties of channel (Tetrahedral)</b>	
Maximum element size	0.03 cm
Minimum element size	0.01 cm

Figure 3-8 represents the “user define” meshing option used to describe the channel cell prototype results. A pre-set tetrahedral mesh for the channel and a fine net “edge boundary meshing” for the electrode, which is very different to the default automatic mesh shown in Figure 3-9. As mentioned by Cutress [43], the limit with meshing, as with finite difference systems, is directly related to the physical memory of

the computational system used for the simulations. However, some people found that increasing the grid size in the numerical simulation would not change the results significantly [40].

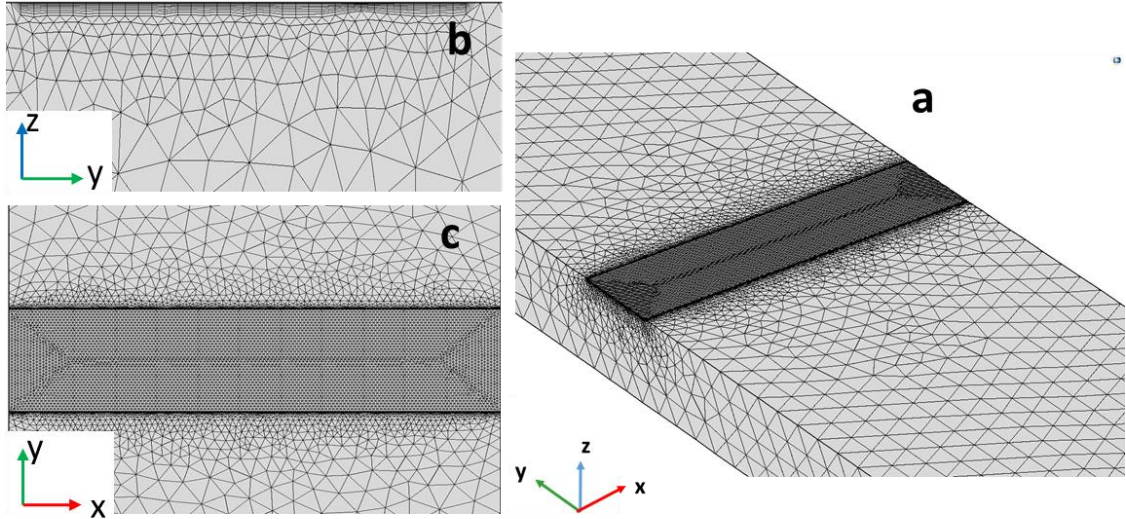


Figure 3-8: CFC user defined meshing (manual): (a) 3D channel cell meshing, (b) zy plane at the corner of electrode, (c) yx plane at the surface of electrode.

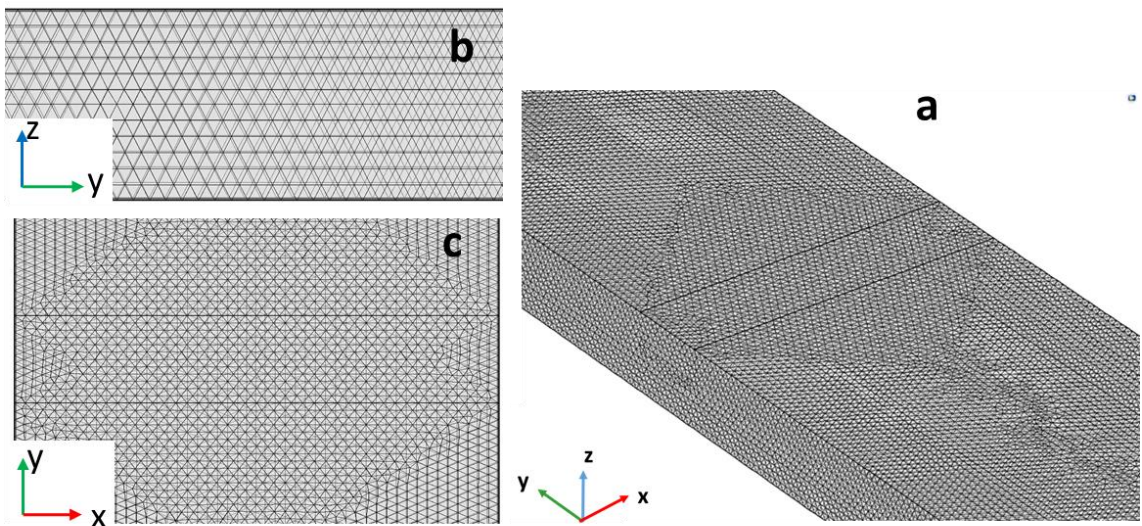


Figure 3-9: CFC user defined meshing (manual): (a) 3D channel cell meshing, (b) zy plane at the corner of electrode, (c) yx plane at the surface of electrode.

The limiting current values obtained with two different mesh models at different flow rates from 14 and 18  $\text{cm}^3\cdot\text{min}^{-1}$  after assuming the concentration of the electroactive species on the electrode surface is equal zero are summarized in Figure 3-10. The hydrodynamic constants obtained for the “auto mesh” and the “manual mesh” were 1.07 and 0.964, respectively. A 7.3% greater than the experimental value for the band electrode (0.997) in the case of the “auto mesh” and 3.3% for the “manual” mesh option. As it was expected, the manual mesh performed better, despite it could be optimized with a different mesh size. The differences with the Levich equation are greater, but the assumptions made in the derivation of this equation do not necessarily apply for the case of this electrode configuration because the effect of the channel side walls on the flow pattern is not taken into account in the analytical solution; the best mesh can only be selected by comparison with experimental data. Figure 3-11 compares the experimental limiting current data (Figure 3-5) with simulation values obtained with the user-defined (manual) mesh (Figure 3-8) at volume flow rates between 6 and 18  $\text{cm}^3\cdot\text{min}^{-1}$ . As expected the self-defined mesh (smaller net) does a better job than then the Levich equation for the reasons discussed above.

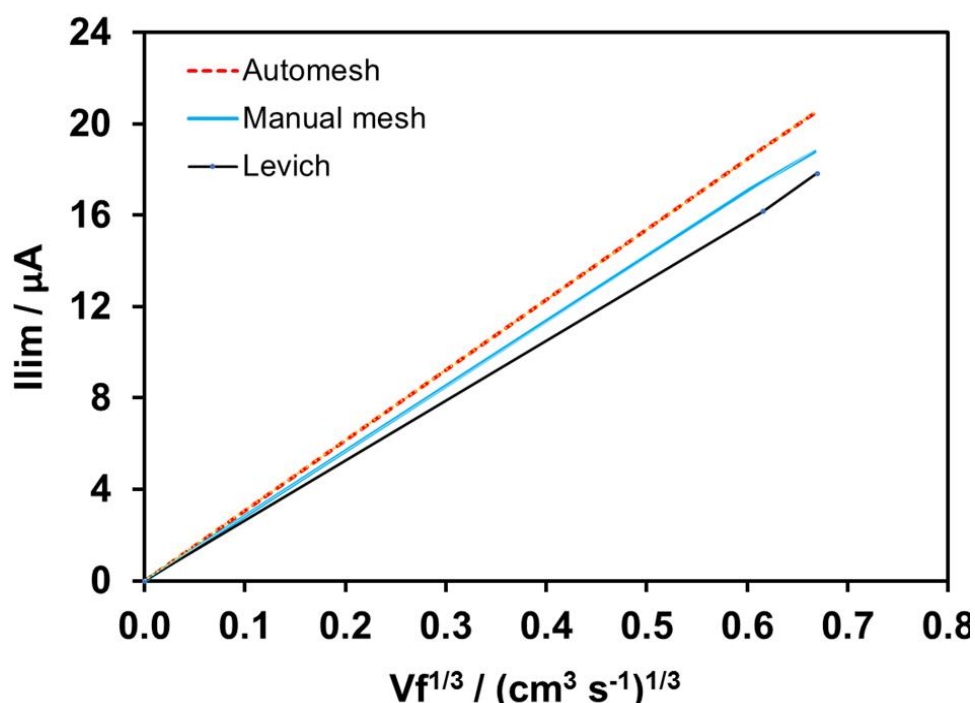


Figure 3-10: comparison between different meshing, users defined meshing with higher granularity and auto-meshing for a band electrode.

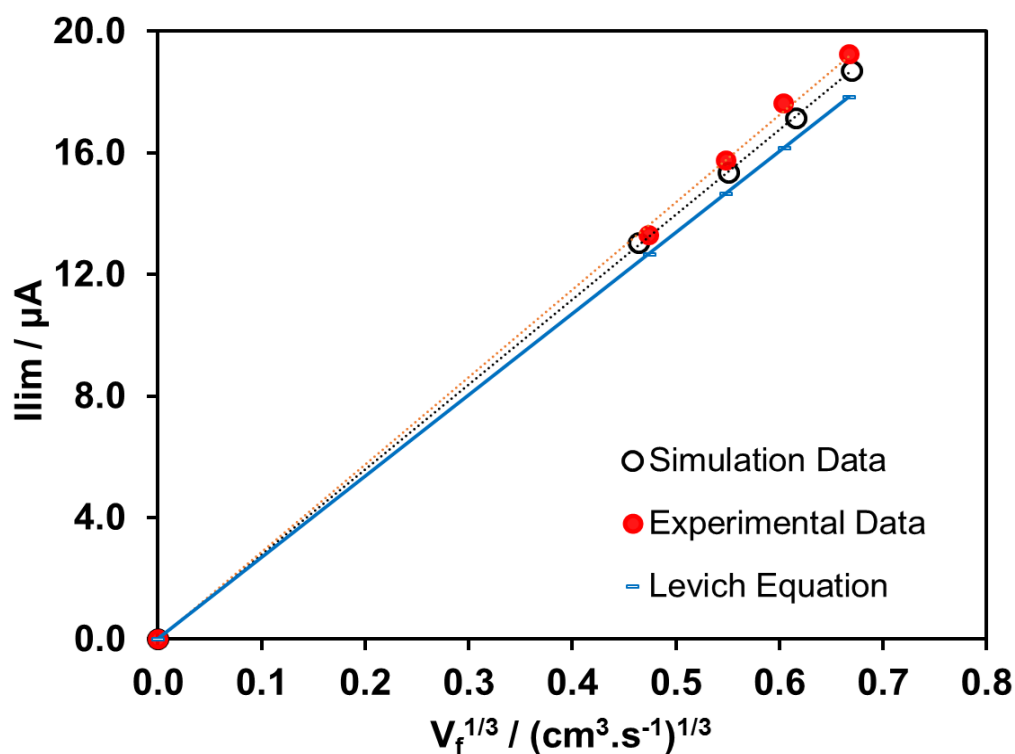


Figure 3-11: (a) Limiting current for the oxidation of 0.95 mM ferrocyanide, (b) Comparison of the simulated  $I_{\text{lim}}$  ( $\circ$ ) to the Levich equation (—) and the experimental data ( $\bullet$ ) for a band electrode ( $w=4\text{mm}$ ,  $x_e=1\text{mm}$ ,  $2h=1\text{mm}$ ) at  $20\text{ mV} \cdot \text{min}^{-1}$  at  $V_f$  values of 6, 10, 14, 18  $\text{cm}^3 \cdot \text{min}^{-1}$ .

The mesh size was reduced and the number of mesh layers (channel) increased to get more accurate results, but there was a limit at which converge could not be achieved. The problem could be due to limitations imposed by the computer used for the numerical simulations [43]. Once the best “practical” mesh was selected, the velocity and concentration profile in the channel, as well as the LSV traces for the oxidation of ferrocyanide at different flow rates were compared with those obtained by other groups for channel cell electrode systems.

### 3.4.2.3 Velocity and Concentration Profile in the Simulated Channel Cell

The velocity profile obtained after solving the *Navier-Stokes* and *continuity* equations with the boundary conditions in Table 3-2 and the “self-define” manual mesh is illustrated in Figure 3-12.

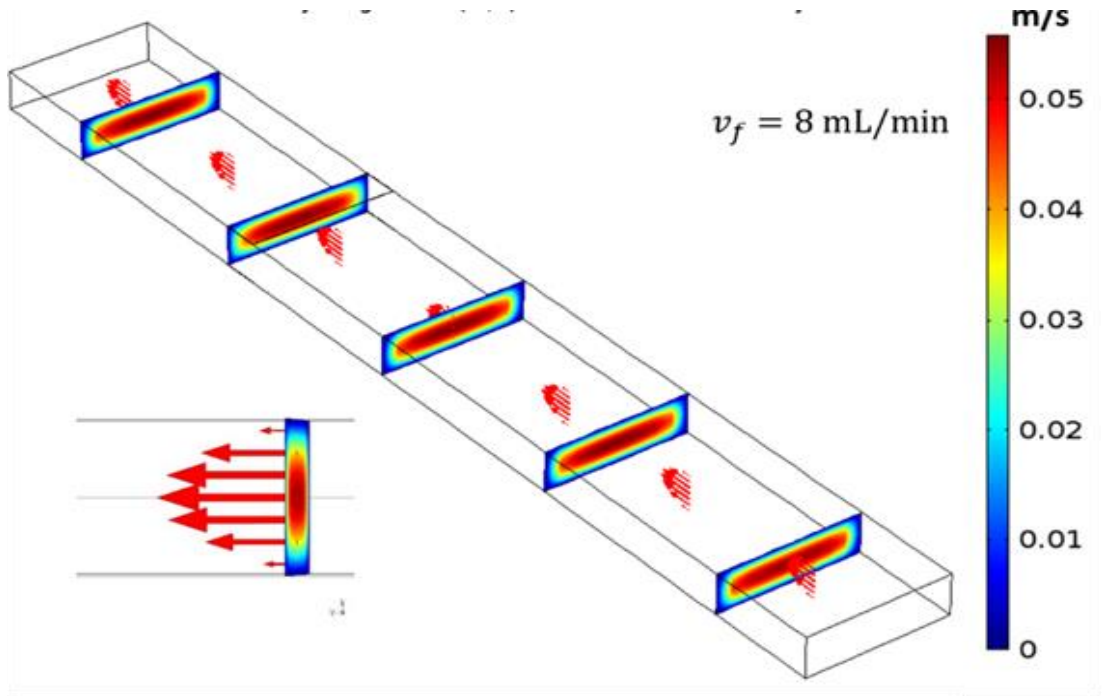


Figure 3-12: Velocity profile obtained by solving Naiver-Stock equation under laminar flow condition ( $V_f = 8 \text{ cm}^3 \cdot \text{min}^{-1}$ ).

A parabolic velocity profile is develop after some distance from the inlet region, in this calculations the inlet has the dimensions of the channel, but this will be changed in the future to include the actual inlet and outlet configurations. The velocity is zero at the channel walls (blue) and maximum at the center (red) in excellent agreement with other studies [25, 42]. The distance from the inlet ( $l_e$ ) required to establish this flow profile is given by:

$$l_e = 0.1 h R_e \quad 3-4$$

The *Reynolds* number (Eq. 2-18) can be estimated via the following equation for a channel cell [25];

$$R_e = \frac{2h v_m}{\nu} \quad 3-5$$

where  $v_m$  ( $\text{cm} \cdot \text{s}^{-1}$ ) is the mean solution velocity ( $\text{cm} \cdot \text{s}^{-1}$ ) which can be obtained using Eq. 3-3 and  $\nu$  is kinematic viscosity.



For the flow rate region explored in the low temperature studies ( $1$  to  $20 \text{ cm}^3.\text{min}^{-1}$ ), the maximum  $Re$  number is equal to  $125$ ; one order lower than the critical Reynolds number ( $2000$ ) for the transition between laminar and turbulent flow [25]. In the case of a thinner channel, smaller  $h$  values, a smaller distance will be required to reach laminar flow and the linear flow rates will be higher than those in the room temperature prototype. For these reasons, it is important to keep this in mind when designing the HT-CFC to keep the  $Re$  numbers under  $2000$ . Another important factor to take into account is the decrease in the viscosity of water with temperature (Figure 3-13). For instance, the  $Re$  number at a flow rate of  $14 \text{ cm}^3.\text{min}^{-1}$  is  $93 \%$  higher at  $250^\circ\text{C}$  than it is at  $25^\circ\text{C}$  for the same channel.

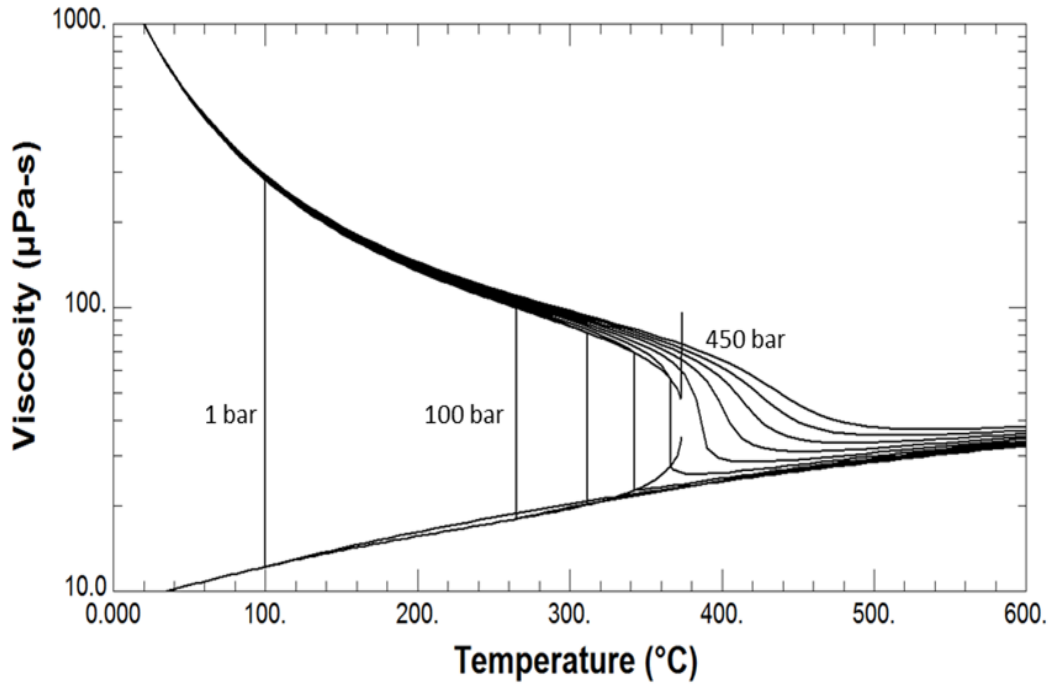


Figure 3-13: Viscosity of water vs. temperature plot at several pressures (Data were taken from REFPROP (version 8)-NIST).

#### 3.4.2.4 Concentration Profile in a Channel Cell

The concentration profile for the electroactive species as a function of the axial distance from the electrode surface is shown in Figure 3-14. The diffusion layer thickness ( $\delta$ ) obtained from the simulated concentration profiles in Figure 3-14 for a volume flow rate of  $18 \text{ cm}^3.\text{min}^{-1}$  is  $\sim 16 \mu\text{m}$ , the value is in very good agreement with those summarized Figure 3-6.

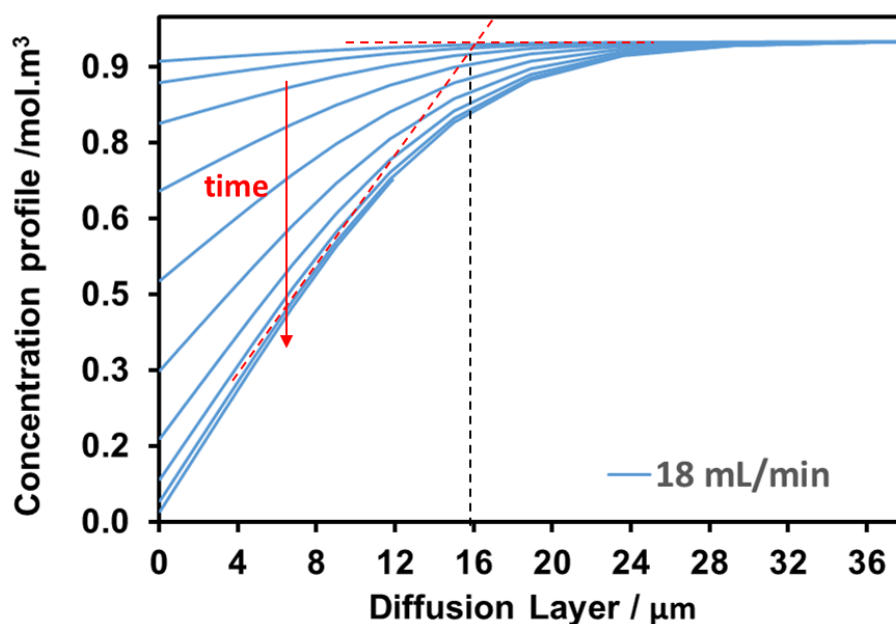


Figure 3-14: Concentration profile on the surface of electrode and diffusion layer thickness.

Figure 3-15 shows the concentration gradient ( $\text{mol.cm}^{-3}$ ) for the electroactive species at the surface of the electrode for volume flow rate  $18 \text{ cm}^3.\text{min}^{-1}$ .

In the case of accessible uniform electrodes, such as the RDE, convection and diffusion are acting in the same direction so, the diffusion layer thickness is constant across the electrode surface [25]. In the case of the CFC, the linear flow velocity in the direction of the flow is a function of the distance to the electrode and it is maximum at the centre of the channel resulting in a diffusion layer which spreads out more slowly further away from the electrode the electrode in the direction of the flow.

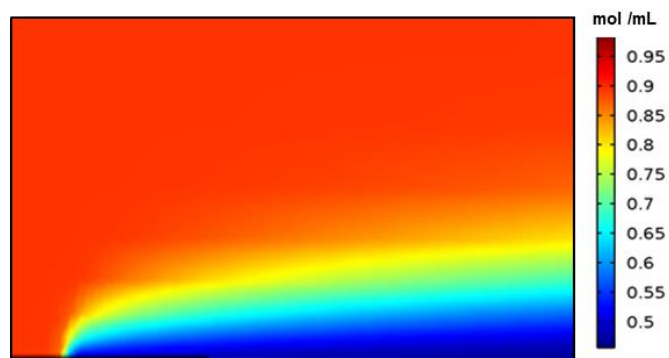


Figure 3-15: Concentration gradient ( $\text{mol.cm}^{-3}$ ) of electroactive species at the surface of electrode, at  $18 \text{ cm}^3.\text{min}^{-1}$ .



### 3.4.3 First Steps Toward the Construction of an HT-CFC

Most of the problems associated with the implementation of an HT-CFC have been addressed, and possible solutions will be discussed in the following sections.

#### a) Cell Dimensions

The dimensions of the RT-CFC prototype were selected with the aim of reaching reasonable mass transfer coefficients ( $D/\delta$ ) under laminar flow conditions ( $Re < 2000$ ). However, after analyzing the room temperature experimental results and the simulation data, it was clear that a smaller cell could perform better at high temperature. An HT-CFC cell was intended in titanium, but it could not be finally tested because of problems with the WE design. The channel in this new cell is 0.3 cm×0.05 cm vs. 0.4 cm×0.1 cm in the RT-CFC. The diffusion layer thickness ( $\delta$ ) (Eq. 3-2) and the mass transfer coefficients ( $D/\delta$ ) for hydroquinone for the two cell configurations at a “nominal” volume flow rate of 10 cm<sup>3</sup>.min<sup>-1</sup> are summarized in Table 3-5.

Table 3-5: Calculated Reynolds numbers and diffusion layer thickness for hydroquinone at temperatures between 25 and 250 °C at 150 bar for a nominal volume flow rate at room temperature equal to 10 cm<sup>3</sup>.min<sup>-1</sup> and two CFC configurations.

Mass Flow rate (gr.cm <sup>-3</sup> )	T (°C)	V <sub>f</sub> (cm <sup>3</sup> .min <sup>-1</sup> )	v (cm <sup>2</sup> .s <sup>-1</sup> ) ×10 <sup>3</sup>	Re	δ (μm)	D/ δ (cm.s <sup>-1</sup> ) ×10 <sup>3</sup>	RDE (rpm)
<b>RT-CFC prototype</b>							
<b>10</b>	25	10.00	17.62	18.92	17.77	4.16	775
	50	10.13	5.53	61.06	23.80	7.56	531
	100	10.43	2.95	117.83	26.97	10.01	439
	150	10.89	2.01	181.02	29.79	12.76	398
	200	11.54	1.57	245.01	37.30	21.18	381
	250	12.47	1.34	310.16	41.78	28.72	380
<b>Tentative HT-CFC</b>							
<b>10</b>	25	10.00	17.62	31.5	10.17	7.28	2365
	50	10.13	5.53	101.8	13.62	13.22	1621
	100	10.43	2.95	196.4	15.44	17.49	1341
	150	10.89	2.01	301.7	17.05	22.29	1214
	200	11.54	1.57	408.3	21.35	37.00	1162
	250	10.00	1.34	516.9	23.91	50.18	1161

The diffusion coefficient of hydroquinone at each temperature and pressure (150 bar) were taken from Ref [5] and the density and viscosity of water data from Refprop (Version 8) from NIST. The mass transfer coefficient are significantly higher in the HT-CFC prototype. However, the  $Re$  numbers are still below the limiting value for the transition from laminar to turbulent flow. The equivalent RDE rotation speeds were included for comparison since this system is more widely known.

#### **b) Construction Materials**

The list of materials that have been used in the construction of high T,p spectroscopic and electrochemical cells includes: alumina [5], titanium[54], platinum [55], Inconel 625 [1], Hastelloy [1, 56], etc.. Many of these materials have shown problems when used under extreme temperature and pressure conditions in the presence of acids or bases under oxidizing or reducing conditions. Alumina does not show the chemical inertness in hot water that is required for these studies. Also it is somewhat brittle and has a tendency to break under high pressure conditions at high temperature. Other materials such as SS 316, Inconel 625, Hastelloy, or Monel were unsuccessful according to studies carried out by Bard's group at the University of Texas [5].

Titanium is an excellent candidate after passivation in the presence of oxygen at 400°C; however, it can be corroded under reducing conditions. Other materials such as platinum and gold can perform better in terms of inertness, but because of the cost and their mechanical properties, the cells' designs are usually more complicated and overall more expensive.

#### **c) The Working Electrode (WE)**

The design of the WE is strongly dependent on the T and p conditions. Polymeric materials, such as Kel-F or PEEK has been used for experiments up to 90 - 110 °C [33] and 150 °C [12] with some success. At higher temperatures, some ceramic materials have been used, but the geometry and requirements were entirely different. It is worth noting that the thermal expansion of these materials must match that of the working electrode to avoid the formation of crevices and an ill-defined electrode area. Indicative thermal expansion coefficients values for Pt, Au, W, alumina, YSZ, quartz and sapphire at given in Table 3-6.

Table 3-6: Thermal expansion coefficient for potential materials as working electrode and electrode support.

Materials	Thermal Expansion Coefficient /( K <sup>-1</sup> )	Source
<b>working electrode</b>		
Pt	8.8–9.1	[57]
Au	13-15	[57]
<b>working electrode support</b>		
Alumina	11-14	[58, 59]
Quartz	0.59	[58, 59]
Sapphire	5.3	[58, 59]

In this thesis, three options have been explored: (i) a machinable ceramic, (ii) a ceramic coating on a metal plate, and (ii) metal electrode sputtered on sapphire.

The first option was eliminated after some time because the electrode could not be embedded in the ceramic, and it had to be glued using a high temperature epoxy (< 200°C). Also, the presence of three different materials and interfaces: metal, epoxy, and ceramic could be a problem when working at high pressure. Furthermore, the cost of a single ceramic plate (~ \$1,000) was considered too high for a test like this considering the problems.

A ceramic coating on a metal plate is an option, but it must satisfy a number of requirements: (i) zero porosity, (ii) excellent adherence, (iii) similar thermal expansion coefficient to that of the electrode, (iv) good mechanical properties under pressure/compression, and (v) it must be an electrical insulator when in contact with water under high temperature conditions. There are facilities with the capability of doing this kind of work, but the development of the electrode is a thesis per se, and this option could not be explored in the framework of this thesis.

The third and final option, the deposition of a very thin film of gold on a non-electrical conductive substrate was investigated in the past for other applications [60-63]. Magnetron sputtering was used for depositing Pt films on fused quartz and alumina with good adhesion in a wide temperature range in gas phase [60, 62]. Chemical vapor deposition, CVD, [64] and electrodeposition [65] of Pt were also investigated by other groups, but the results were not entirely successful due to impurities in the films. In

addition, in most of these studies, little information is provided about the adherence of the films after or before immersion.

In this study, we explored the possibility of using a gold film sputtered on a sapphire substrate using an NSC-1000 sputtering system from Nano-Master Inc. available at the University of Toronto. The gold film ( $\sim 500$  nm) was deposited on top of a thin layer of chromium ( $\sim 3$  nm) deposited on sapphire. Unfortunately, the adherence was extremely poor, but there are many possible reasons for the observed behavior and it will be investigated as part of a future project.

### **3.5 Conclusions**

A commercial software (COMSOL MP) was identified and used for the simulation of LSV experimental data for the oxidation of ferrocyanide in 0.1M KCl at room temperature obtained with a CFC prototype. The results have been used to optimize the design of the cell and the working electrode, as well as the geometry of the channel.

Different electrode/support systems have been analyzed without significant success. However, the possibility of using a ceramic substrates coated with a glass thin film (to reduce porosity) with a gold electrode sputtered on the surface is considered one of the most promising options. Other option, that can be use is sapphire as support and treatment the surface to improve the adherence of Pt or Au.

## Chapter 4: Redox Couples for High T,p Electrochemical Studies

### 4.1 Introduction

An analysis of the high temperature electrochemical studies carried out by other research groups showed the oxidation of H<sub>2</sub>Q to BQ (Eq. 4-1) seems to fulfill the stability requirements for the evaluation of an HT-CFC.



Bard's study [3] has shown H<sub>2</sub>Q has a good chemical stability at low pH without any decomposition up to 374°C and 170 bar, as long as O<sub>2</sub> is not present; because BQ (the reaction product) can decompose in the presence of water under high temperature conditions [66-68]

Ragimov et al. [66, 67] found BQ polymerizes in nitrogen-saturated water at temperatures as low as 50 °C with the formation of H<sub>2</sub>Q. Based on the amount of polymer and H<sub>2</sub>Q formed at different temperatures and during different periods of time, the authors were able to propose a mechanism for polymerization and a kinetics model. Since BQ was unable to polymerize in organic solvents below 220 °C, the authors concluded an activation step involving H<sub>2</sub>O or OH<sup>-</sup> was required to initiate the polymerization process. These results are important, but the pH of the H<sub>2</sub>Q solutions used for the determination of the diffusion coefficients of H<sub>2</sub>Q up to the critical point of water in ref. [3] are significantly more acidic (0.1 M NaHSO<sub>4</sub>).

Recently, Xu et al. [68] studied the role of supercritical water (SCW) on the mechanism of decomposition of benzoquinone at 400°C and 250 bar in the absence of oxygen. They showed that under SCW conditions, BQ is reduced to HQ and char; but neither 2-hydroxyl-p-benzoquinone nor 2,5-dihydroxyl-pbenzoquinone were produced at

high temperature as proposed by Ragimov. According to the authors, the polymerization of BQ (char) generates hydrogen radicals and release  $H_2$  that leads to the reduction of BQ to  $H_2Q$ . Since polymerization had to take place in order to generate any of these two species ( $H\bullet$  or  $H_2$ ), the conversion of BQ to  $H_2Q$  is not stoichiometric, the yield of  $H_2Q$  under these conditions is equal to 37% and 43% after 2 and 4 hours, respectively. The authors also reported data for the decomposition of BQ in deoxygenated water at 200, 300 and 350 °C and saturation pressure. The results were difficult to explain since the decomposition yields are similar to those in SCW, and the differences in decomposition and yield between temperatures was tiny.

Considering the residence time of the solutions at high temperature in a typical CFC, an obvious question is whether BQ can withstand the experimental conditions within the timeframe of an experimental run. Because of the lack of experimental data in acidic media, the question can only be answered by studying the thermal stability of BQ and  $H_2Q$  under similar conditions.

In this work, UV-visible spectroscopy has been used to investigate the thermal stability of  $H_2Q$  and BQ at temperature and pressure up to 250°C at 70 bar. To the best of our knowledge, this is the first time these systems has been studied under hydrothermal conditions using this technique.

## **4.2 Experimental Section**

### **4.2.1 Chemicals**

All chemicals were purchased from Sigma-Aldrich at the highest grade available and used without further purification. BQ (1,4-benzoquinone,  $\geq 98\%$ , Sigma-Aldrich),  $H_2Q$  (hydroquinone,  $\geq 99\%$ , Sigma-Aldrich), and sodium bisulfate monohydrate ( $NaHSO_4 \cdot H_2O$ , 99%, Sigma-Aldrich). Solutions were prepared by mass using free oxygen deionized water with a resistivity of 18 M $\Omega$ .cm that it was prepared by bubbling argon gas (Praxair, GP-520078A) in an air-tight bottle overnight. The concentrations of benzoquinone and hydroquinone in the solutions were kept within  $10^{-4}$  and  $10^{-5}$  molal to avoid extremely high absorbance values. A supporting electrolyte, 0.2 molal  $NaHSO_4$ , was used to mimic the composition utilized in the electrochemical studies in ref. [5].

#### 4.2.2 High T,p UV-visible Spectroscopic Cell and Injection System

The UV-visible system used to carry out these experiments (Figure 4-1) is similar to the one used in previous studies [54, 69]. A picture of the experimental setup is shown in Figure 4-2.

The injection system is composed of a high-pressure (ISCO D-Series) pump (1), used to circulate water through the system at a constant flow rate ( $1 \text{ cm}^3/\text{min}$ ) under high pressure conditions; a titanium six-port valve (2) that allows to inject the solution under study into the titanium pre-heater (3); a high T,p UV-visible cell with sapphire windows (4); two on-off valves that can be used to isolate the cell for studies without flow (5); a cooler (6); and a back-pressure regulator (7) from Vici-Valco (Model 26-1700) at the end of the high pressure line to keep the solution (or water) under high pressure conditions. The cell and pre-heater were heated using an OMEGA temperature controller (model CSC32). A thermocouple was used to control and measure the temperature of the cell. The pressure was set at 100 bar to ensure the solvent was in liquid phase in the entire temperature range.

Because the PEEK (polyetheretherketone) loop ( $80 \text{ cm}^3$ ) used to inject the solution into the cell is relatively large, a low-pressure peristaltic pump (Masterflex L/S economy drive) was used to fill the sample loop from a free oxygen bottle containing the  $\text{H}_2\text{Q}$  or BQ solutions. Overall the system resembles a high-performance liquid chromatography (HPLC) system with the exceptions of the bigger injection loop and the high T,p cell ( $\sim 0.34 \text{ cm}^3$ ) instead of the column. Only PEEK, PTFE and titanium were in contact with the solutions.

A Cary 50 spectrophotometer (190–1100 nm) was used to record the absorption spectra at temperatures between  $25^\circ\text{C}$  to  $250^\circ\text{C}$ . All spectra were collected at 1 nm wavelength interval from 200 nm to 800 nm at a scan rate  $2400 \text{ nm}\cdot\text{min}^{-1}$  using Cary Win UV scan Application software.

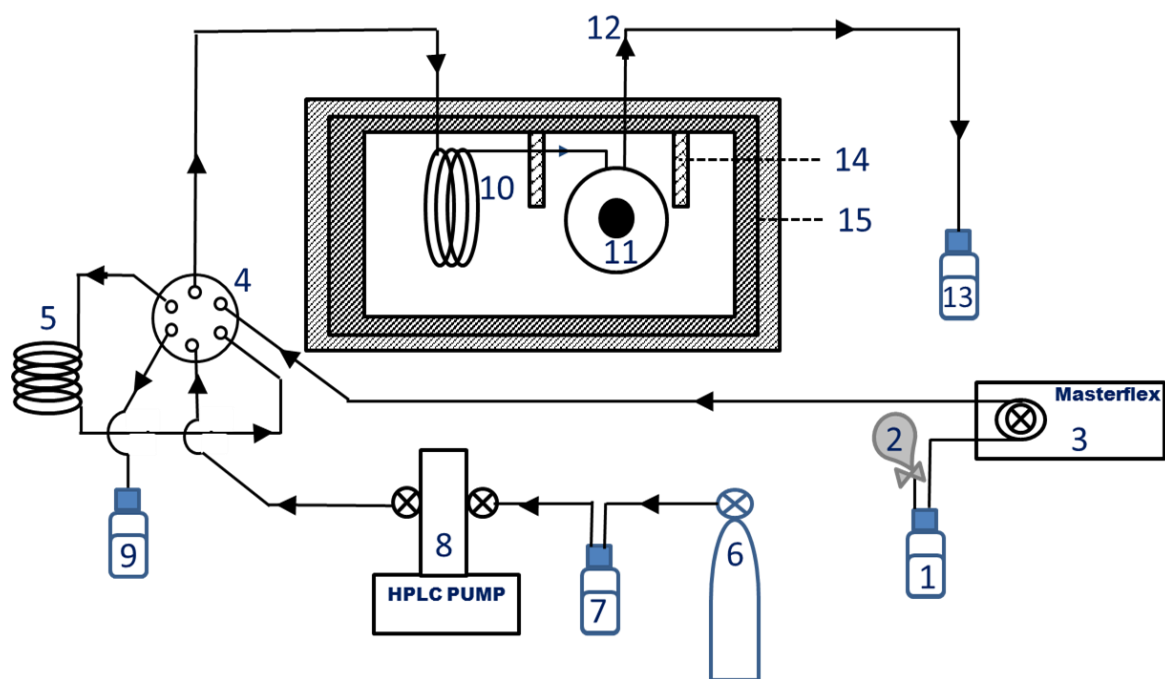


Figure 4-1: UV-visible flow cell and high-pressure injection system, (1) solution, (2) nitrogen balloon, (3) peristaltic pump, (4) six port valve, (5) PEEK injection loop, (6) nitrogen gas, (7) deionized water, (8) HPLC pump, (9) waste, (10) titanium preheater, (11) titanium cell, (12) outlet, (13) waste, (14) heater, and (15) ceramic insulation.

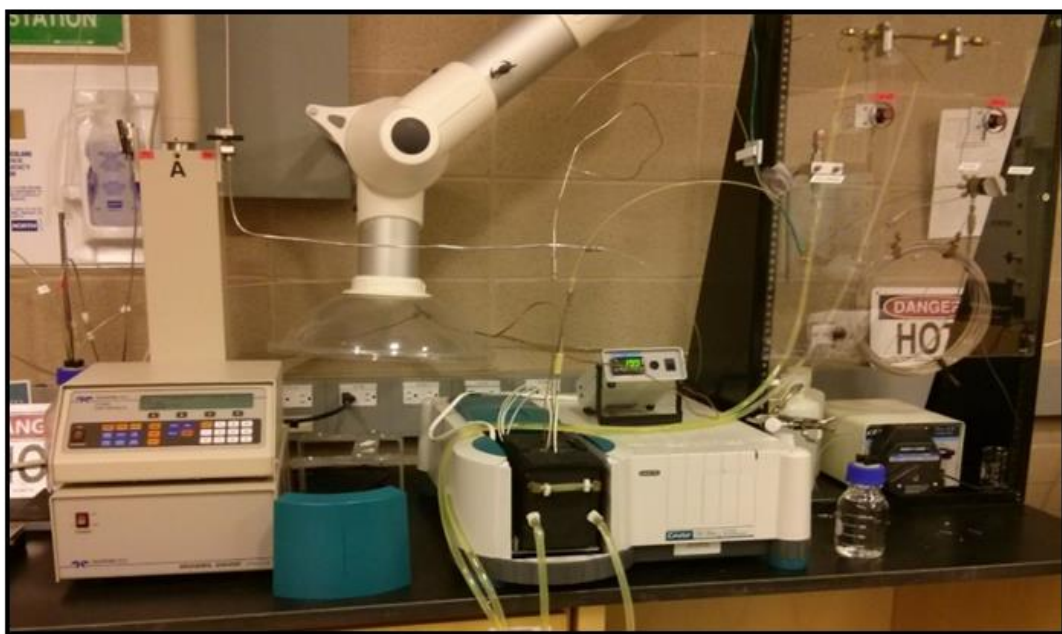


Figure 4-2: Picture of the high T,p UV-Vis spectroscopy system used for studying the thermal stability of H<sub>2</sub>Q and BQ.



#### 4.2.3 Procedure Adopted for Collecting the Absorption Spectra

Figure 4-3 illustrates the changes observed in the UV-Vis spectra of hydroquinone at 100°C just after injecting the solution into the cell.

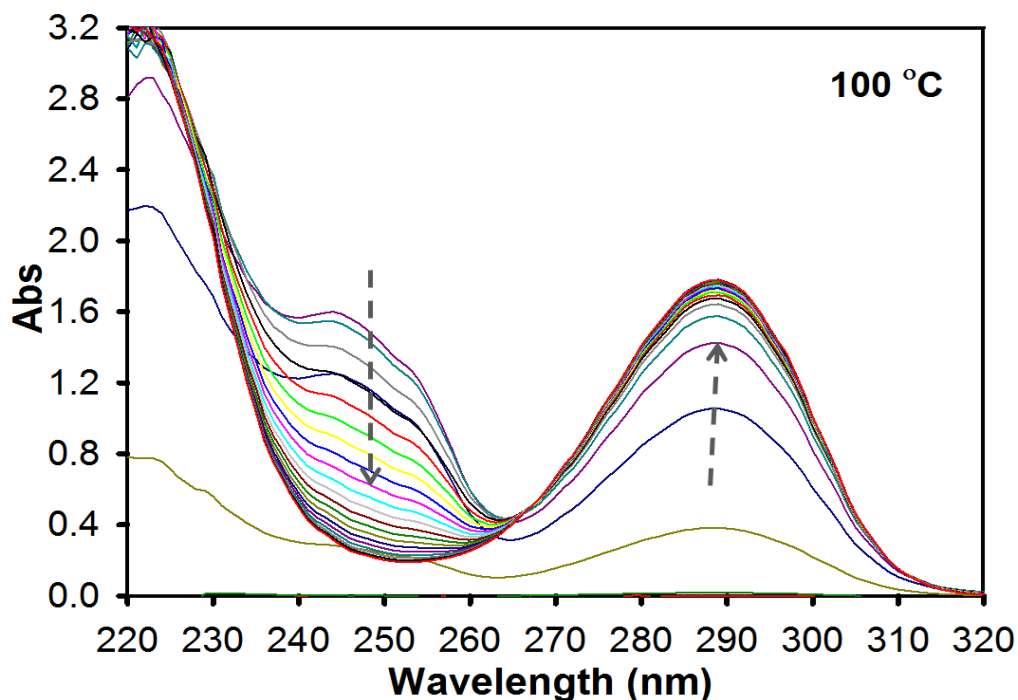


Figure 4-3: Baseline-corrected absorbance data for 0.3 mM H<sub>2</sub>Q in 0.2M NaHSO<sub>4</sub> at 100°C in titanium cell. Arrows indicate the evaluation of the spectra upon time after injection.

As shown, the most distinctive feature of the spectra after injecting the solution into the cell is the presence of both BQ ( $\lambda_{\text{max}} = 244$  nm) and H<sub>2</sub>Q ( $\lambda_{\text{max}} = 289$  nm) due to the presence of trace of oxygen in the first part of the injection loop and partial oxidation of H<sub>2</sub>Q to BQ. As the amount of dissolved oxygen decreases, the signal for H<sub>2</sub>Q increases while the one for BQ decreases. After 15 cycles (~ 15 minutes after the solution injection into the cell), no changes were observed between spectra and only one peak with a maximum at around 289 nm due to H<sub>2</sub>Q was observed. The fact that the absorbance at this wavelength does not change upon time is also an indication that water have been displaced, and the concentration of H<sub>2</sub>Q in the cell is equal to that in the original solution. The same applies for other temperatures. Spectra for BQ and H<sub>2</sub>Q were collected 15 minutes after injection to ensure the solution in the cell was identical to that in the bottle.

#### 4.2.4 Analysis of the Spectroscopic Data

The Beer's law for a solution of multiple absorbing species is given by:

$$A(\lambda) = \sum \varepsilon_i(\lambda) b C_i \quad 4-2$$

where  $A(\lambda)$  and  $\varepsilon_i(\lambda)$  ( $\text{dm}^3/\text{mol}\cdot\text{cm}$ ) are the absorbance and the molar absorptivity of the absorbing species at a wavelength,  $\lambda$ , respectively.  $C_i$  ( $\text{mol/L}$ ) is the molar concentration and  $b$  ( $\text{cm}$ ) is the optical path length.

For convenience, a different concentration scale, specific molality,  $m_i^*$  ( $\text{mol/kg}$  of solution), is commonly used in hydrothermal studies to account for the thermal expansion of the solution as the temperature increase (Figure 4-4). The expression for the Beer's law in terms of specific molality is given by;

$$A(\lambda)_m = \sum \varepsilon_{i,m}(\lambda) b m_i^* \quad 4-3$$

where  $A(\lambda)_m$  is the corrected absorbance  $A(\lambda)_m = A(\lambda) / \rho_{\text{solution}}$ . However, the solutions are diluted and for the purpose of this work, the density of the solution was approximated to that of water (REFPROP, NIST) at the same temperature and pressure. The densities of water at 100, 150, 200 and 250 °C at 70 bar used to correct the spectra are listed in Table 4-1.

Table 4-1: Density of water used to correct the absorption spectra.

T(°C)	p (bar)	Density ( $\text{kg}/\text{dm}^3$ )
25	70	0.998
100	70	0.961
150	70	0.920
200	70	0.868
250	70	0.802

### 4.3 Results and Discussion

In this study, the thermal stability of BQ and H<sub>2</sub>Q in acid aqueous media has been investigated using UV-visible spectroscopy at temperatures up to 250° at 70 bar. Despite, there are numerous studies involving UV-visible spectroscopy under ambient conditions because the relevance of quinones in biological systems [70], to the best of our knowledge these are the first UV-visible spectroscopic data at temperatures above the boiling point of water.

Figure 4-4 shows the UV-visible spectra for BQ and H<sub>2</sub>Q in aqueous 0.2 m NaHSO<sub>4</sub> after baseline correction using the spectra of 0.2 m NaHSO<sub>4</sub> solution at the same T and p. The position of the maximum of absorption for BQ (246 nm) and H<sub>2</sub>Q (289 nm) are in excellent agreement with those reported for the same ( $\pi \rightarrow \pi^*$ ) transitions in other studies under ambient conditions [71].

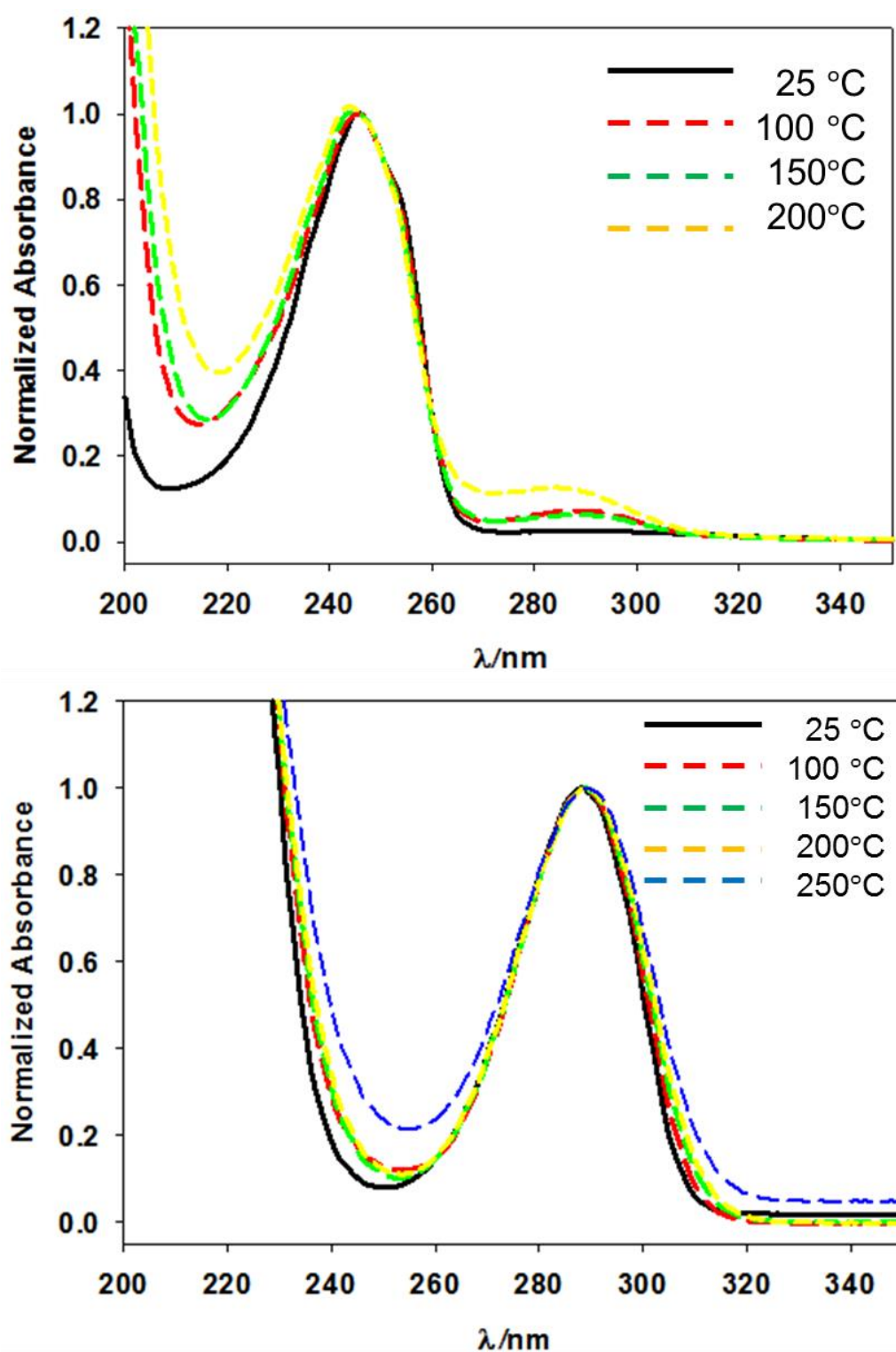


Figure 4-4: Normalized UV-visible absorption spectra for 0.07 mM BQ (top) and 0.3 mM H<sub>2</sub>Q (bottom) in 0.2M NaHSO<sub>4</sub> at 25, 100, 150, and 200 °C and 70 bar. The spectrum for H<sub>2</sub>Q at 250°C and 70 bar (broken blue line) was also included.

#### 4.3.1 Temperature and Pressure Effects on the Spectrum of BQ

The two most distinctive features in the normalized spectra of BQ in Figure 4-4 are: (i) a blue shift as the temperature increases and dielectric constant of water decreases and (ii) a new absorption band between 260 and 300 nm at temperatures higher than 100 °C. The blue shift in Figure 4-4 can be better seen in Figure 4-5. A similar behaviour was observed by Ahmed and Khan [71] while studying the solvent effect on the absorption spectra of benzoquinones. The changes were assigned to changes in the solvent-BQ interaction that results in a stabilization of the excited state and a reduction in the energy gap between excited and ground state. An analysis of the solvents studied by Ahmed and Khan shows some of them have dielectric constants similar to that of water at high T,p allowing a comparison between studies. Table 4-2 illustrates the effect of solvent dielectric constant on the  $\pi \rightarrow \pi^*$  transition energy, despite the numbers are different, the trend is the same in both studies.

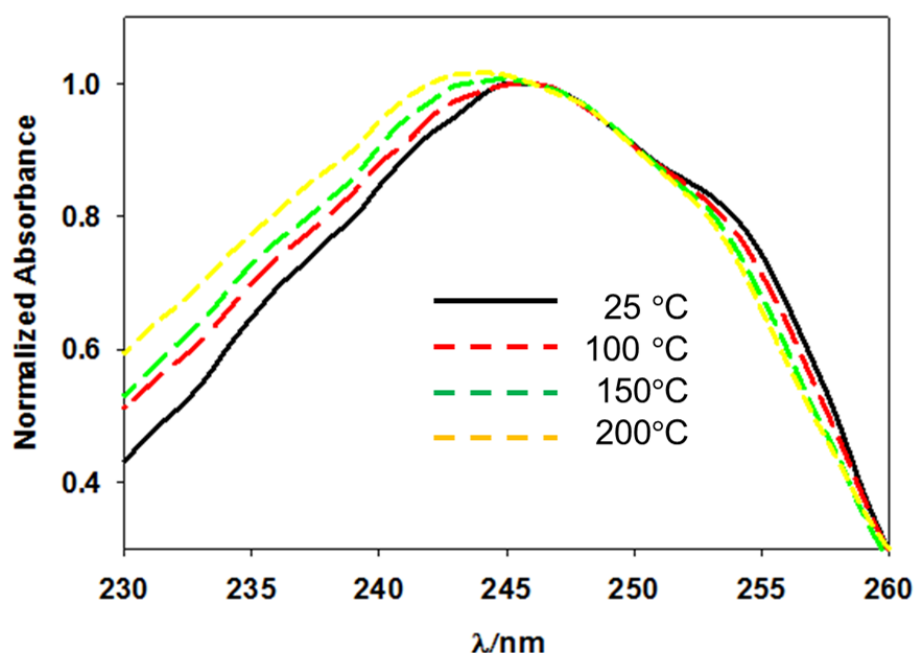


Figure 4-5: Normalized UV-visible absorption spectra for 0.07 mM BQ: Blue shift in the wavelength of the maximum absorbance with temperature (25, 100, 150, and 200 °C at 70 bar).

Table 4-2: Effect of dielectric constant of the solvent on the wavelength of the maximum of absorption fo BQ.

T(°C)	p(bar)	$\epsilon(\text{H}_2\text{O})^a$	$\lambda_{\text{max}}$ (nm) (This study)	Solvent/ $\epsilon(\text{solvent})^b$	$\lambda_{\text{max}}^b$ (nm)
25	1	78.46	246	Water	246
100	70	57.69	246	---	---
150	70	46.28	245	Glycerol /42.5	246
200	70	37.28	244	Acetonitrile/37.5	242
250	70	30.03	---	Methanol/32.7	243
---	---	---	---	---	----
---	---	---	---	Iso-octane/1.94	240

<sup>a</sup> Uematsuet al. [72].

<sup>b</sup> Ahmed et al. [71].

The changes in the spectrum of BQ can be better appreciated as a difference spectrum by using the spectrum at 100 °C as a reference,  $A(T) - A(100\text{ °C})$ . The results are summarized in Figure 4-6. The negative absorption bands in the difference spectra are due to BQ decomposition, and the absorbance with temperature. The decomposition of BQ that starts to be noticeable at temperature as low as 100 °C (Figure 4-3) and it is completed after a minute at 250 °C (Figure 4-6). The positive absorption bands are due to the formation of a new species. The excellent agreement between the position of the new band with that for H<sub>2</sub>Q between 260 and 300 nm in Figure 4-4 is a confirmation of the presence of H<sub>2</sub>Q in the solutions.

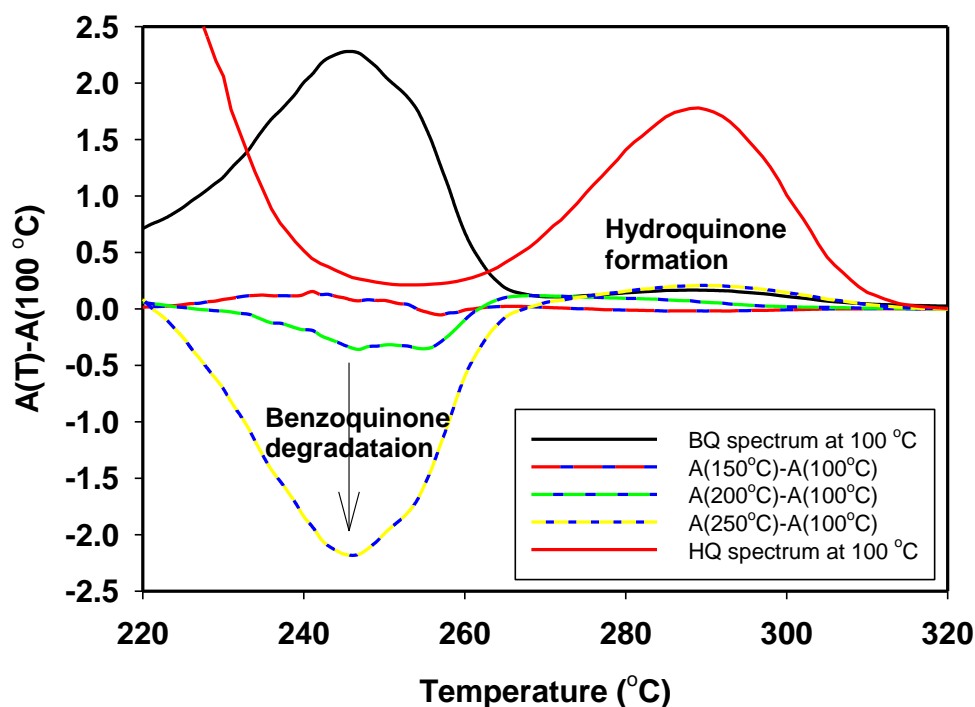


Figure 4-6: Difference spectra ( $A(T) - A(100^\circ\text{C})$ ) for 0.07 mM BQ in 0.2 M  $\text{Na}_2\text{HSO}_4$  at 150, 200, and 200 °C and 70 bar. Reference spectrum: 0.07 mM BQ at 100 °C. Spectra corrected to account for thermal expansion of the solution.

#### 4.3.2 Temperature and Pressure Effects on the Spectrum of HQ

The similarities between the normalized absorption spectra of  $\text{H}_2\text{Q}$  in Fig. 4-4 are an indication of the higher thermal stability of  $\text{H}_2\text{Q}$  compared to BQ. The solvent dielectric constant effect on the energy of the transition is also small in the case of  $\text{H}_2\text{Q}$  since the position of the maximum of absorbance at 289 nm does not show any significant change between 25 and 250 °C, despite the dielectric constant of water at the highest temperature is 62% smaller than at room temperature.

In contrast with BQ, the changes in the difference spectra ( $A(T) - A(100^\circ\text{C})$ ) of  $\text{H}_2\text{Q}$  are negligible at 150 and 200 °C (Figure 4-7). Even the difference at 250 °C can be due to the presence of oxygen since a leak was observed when completing the experiments.

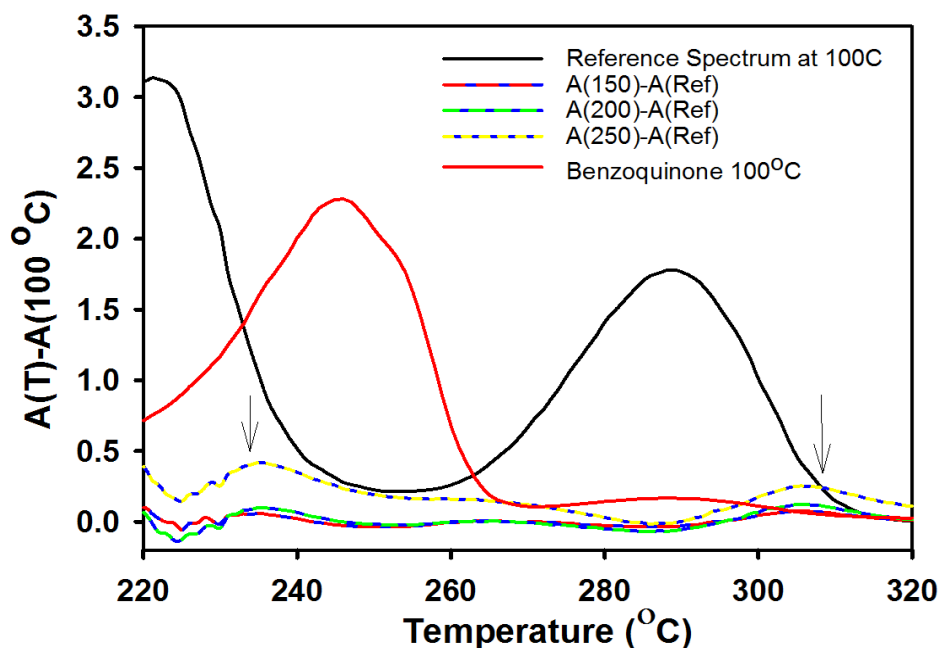


Figure 4-7: Difference spectra ( $A(T) - A(100^{\circ}\text{C})$ ) for 0.3 mM  $\text{H}_2\text{Q}$  in 0.2 M  $\text{Na}_2\text{HSO}_4$  at 150, 200, and 250  $^{\circ}\text{C}$  and 70 bar. Reference spectrum: 0.03 mM BQ at 100  $^{\circ}\text{C}$ . Spectra corrected to account for thermal expansion of the solution.

#### 4.3.3 Mechanism of Decomposition and Formation of Other Species

In acid media, BQ undergoes a significant decomposition even at 100  $^{\circ}\text{C}$ . The decomposition process results in the formation of  $\text{H}_2\text{Q}$  and a non-absorbing compound, likely a BQ condensation product based on Razimov et al.[67] and Xu et al. [68] studies.

Razimov et al.[67] found BQ undergoes polymerization reactions with partial formation of  $\text{H}_2\text{Q}$  in aqueous solutions at temperatures below 100  $^{\circ}\text{C}$ , and the polymerization reactions are accompanied by a significant reduction of pH. By studying the BQ stability in water and in organic solvents as a function of temperature, the authors concluded that  $\text{H}_2\text{O}$ , particularly  $\text{OH}^-$ , plays a significant role in the overall mechanism by forming a complex with BQ that has a more nucleophilic character than BQ itself. Electron transfer from the complex to a free BQ molecule is favorable and results in the formation of free radicals that are involved in the production of polymers and hydroquinone in hot water.

Xu and co-workers [68] have used BQ as a probing compound to investigate the hydrogen donation ability ( $\text{H}^{\bullet}$  and  $\text{H}^+$ ) of SCW in the pyrolysis of carbonaceous compounds because other studies have recognized BQ as a free radical scavenger able to



capture an  $H\bullet$  to form  $H_2Q$  and phenol or an  $OH\bullet$  radicals to form  $H_2Q$ , 2-hydroxyl-BQ, and 2,5-dihydroxyl-BQ. The absence of phenol or other hydroxyquinones in the reaction products allowed them to conclude that hydrogen is a BQ condensation product must be responsible for the reduction of BQ to  $H_2Q$  under SCW at 400 °C and 253 bar. The authors have also studied the stability of BQ under hydrothermal conditions at saturation pressures, and as in the case of SCW, the only reaction products were char and  $H_2Q$ . However, the BQ conversion rate and  $H_2Q$  yields were close to the values observed in SWC (a BQ conversion of ~ 60% after 2 hours and a  $H_2Q$  yield of ~ 37%) something difficult to explain.

The absorption spectra in Figure 4-5 are in good agreement with the decomposition products reported by previous studies. However, the rate of conversion in acid solution is faster than in hot compressed water [67]. At temperatures over 200 °C only a few seconds are required to convert BQ to  $H_2Q$  and char (or other condensation products) and the  $H_2Q$  yields are extremely low when compared with those reported in ref. [68].

There are two main processes that can be responsible for the low observed yields: either  $H_2Q$  is not formed because a competing reaction is consuming hydrogen, or  $H_2Q$  decomposes after forming. Despite the latter is possible, since it is known  $TiO_2$  can catalyze the decomposition of organic compounds under hydrothermal conditions, the UV spectra in Figure 4-7 do not show that.; also the electrochemical studies carried out by Bard's group on the oxidation of  $H_2Q$  up to the critical point of water support these data. If  $H_2Q$  can stand the conditions at least in the timeframe windows of Bard's and our experimental runs, then a competing reaction must be consuming most of the hydrogen formed as a result of BQ condensation reactions. Titanium can absorb hydrogen at high temperature [73]; the formation of  $H_2Q$  will be clearly less favourable in a titanium cell with a titanium pre-heater than in a stainless steel autoclave with a quartz sleeve like that used in ref. [71].

#### 4.4 Conclusions

This study showed the potential of UV-visible spectroscopy as an experimental tool for studying the mechanism of decomposition of benzoquinones under hydrothermal conditions.  $H_2Q$  is quite stable in acid medium up to 200 °C at 70 bar, over this temperature, the decomposition process can be due to the presence of oxygen confirming Bard's group findings. The reduction of BQ to  $H_2Q$  has been confirmed from the absorption spectra of BQ as a function of temperature. The conversion is not quantitative; but the formation of other absorbing hydroxylated quinones was not observed between 100 and 250°C at 70 bar. The formation of benzoquinone is not expected to be a serious problem while studying the oxidation of hydroquinone in a titanium cell, as long as oxygen is not present, otherwise the presence of benzoquinone in the pre-heater will induce the formation of polymeric species and it will result in electrode passivation.

## Chapter 5: Conclusions and Future Work

This thesis describes the work done on the design of an HT-CFC for electrochemical studies under hydrothermal conditions. Several room-temperature cells were analyzed to identify a configuration that could be adapted to high-temperature and high-pressure conditions. Unfortunately, most of the cells consisted of two polymeric blocks (Kel-F, PTFE, Plexiglass or PEEK) bolted together with a PTFE seal in the middle (the channel). Little information was usually provided about the impact of compression on the dimensions of the channel.

The important changes in the mechanical properties of materials like PTFE or Kel-F at temperatures over 150 °C made impossible to use a gasket as seal and channel close to this limit, for this reason a different configuration was adopted for the construction of the first RT-CFC prototype. The new system was used to study the oxidation of ferrocyanide in 0.1M KCl. The LSVs obtained with the RT-CFC were in excellent agreement with those expected for this kind of device with well defined “plateau” in the mass transport control region.

The RT-CFC data were analyzed using COMSOL MP (CFD and electroanalysis modules). The Levich equation for the electrode configuration used in this cell is a good approximation, but the simulation results obtained with a fine mesh around the working electrode were clearly more accurate. The numerical simulation model is one of the outcomes of this thesis work, since COMSOL MP will be used for optimization of the HT-CFC design.

Furthermore, in this work for the first time UV-visible spectroscopy was used to investigate the thermal stability of hydroquinone and benzoquinone in a titanium cell under high p,T conditions. The studies showed H<sub>2</sub>Q in 0.2 M NaHSO<sub>4</sub> can stand temperatures at least up to 250 °C at 70 bar without decomposition in good agreement with previous studies. The oxidation of hydroquinone in acid media fulfills the stability requirements for the evaluation of a future HT-CFC; however, the elimination of traces of oxygen is crucial to avoid the formation BQ and its subsequent decomposition. The formation of BQ polymerization products can contaminate and/or passivate the electrode surface. Also, the

production of hydrogen by polymerization of BQ can be a problem under high T,p conditions if titanium is used for the construction of the cell and the pre-hater.

Despite a large number of materials (machinable ceramics, sapphire, and quartz) have been considered for the working electrode. The problem is still open.

Future work should focus on developing a robust working electrode for the new HT-CFC cell. Because of the dimensions of the working electrode, Au or Pt should be deposited on the surface of quartz, sapphire, or ceramic using sputtering or a similar method. A facility at Waterloo University has been identified for this project.

Depending on the results, the HT-CFC should undergo a full characterization under hydrothermal conditions. The oxidation of hydroquinone is a good candidate for this work, as well as the COMSOL MP model developed as part of this thesis for modeling the high T,p experimental results.

## References

1. Wildgoose GG, Giovanelli D, Lawrence NS, Compton RG. High-temperature electrochemistry: A review. *Electroanalysis* 2004,**16**:421-433.
2. Höffelner W. *Materials for Nuclear Plants, from safe design to residual life assessments*. Oberrohrdorf, Switzerland: Springer; 2011.
3. Kallikragas DT, Plugatyr AY, Svishchev IM. High Temperature Diffusion Coefficients for O<sub>2</sub>, H<sub>2</sub>, and OH in Water, and for Pure Water. *Journal of Chemical & Engineering Data* 2014,**59**:1964-1969.
4. Lemmon E, Huber ML, McLinden MO. *NIST Standard Reference Database 23: Reference Fluid Thermodynamic and Transport Properties - REFPROP*; 2010.
5. Liu CY, Snyder SR, Bard AJ. Electrochemistry in near-critical and supercritical fluids. 9. Improved apparatus for water systems (23-385°C). The oxidation of hydroquinone and iodide. *Journal of Physical Chemistry B* 1997,**101**:1180-1185.
6. Flarsheim WM, Tsou YM, Trachtenberg I, Johnston KP, Bard AJ. Electrochemistry in near-critical and supercritical fluids. 3. Studies of Br<sup>-</sup>, I<sup>-</sup>, and hydroquinone in aqueous solutions. *Journal of Physical Chemistry* 1986,**90**:3857-3862.
7. Lvov SN, Zhou XY, MacDonald DD. Flow-through electrochemical cell for accurate pH measurements at temperatures up to 400 °C. *Journal of Electroanalytical Chemistry* 1999,**463**:146-156.
8. Trevani LN, Calvo E, Corti HR. High-temperature wall-tube cell- Design, characterization and results of mass transport phenomena. *Journal of the Chemical Society - Faraday Transactions* 1997,**93**:4319-4326.
9. Macdonald DD, Lvov SN. Development of advanced in-situ techniques for chemistry monitoring and corrosion mitigation in SCWO environment In; 2000.

10. McDonald AC, Fan FRF, Bard AJ. Electrochemistry in near-critical and supercritical fluids. 2. Water. Experimental techniques and the copper(II) system. *Journal of Physical Chemistry* 1986,**90**:196-202.
11. McBreen j, O'Grady WE, Ritcher R. A rotating disk electrode apparatus for the study of fuel cell reactions at elevated temperatures and pressures. *Journal of the electrochemical society* 1984:1215-1217.
12. Wiberg GKH, Fleige MJ, Arenz M. Design and test of a flexible electrochemical setup for measurements in aqueous electrolyte solutions at elevated temperature and pressure. *Review of Scientific Instruments* 2014,**85**:085105.
13. Gründler P, Kirbs A, Dunsch L. Modern thermoelectrochemistry. *ChemPhysChem* 2009,**10**:1722-1746.
14. Moorcroft MJ, Lawrence NS, Coles BA, Compton RG, Trevani LN. High temperature electrochemical studies using a channel flow cell heated by radio frequency radiation. *Journal of Electroanalytical Chemistry* 2001,**506**:28-33.
15. Qiu F, Compton RG, Marken F, Wilkins SJ, Goeting CH, Foord JS. Laser activation voltammetry: Selective removal of reduced forms of methyl viologen deposited on glassy carbon and boron-doped diamond electrodes. *Analytical Chemistry* 2000,**72**:2362-2370.
16. Corti H, Fernández-Prini R. Behaviour of the mercury, mercuric oxide electrode in alkaline solutions in the temperature range 298–363 K. *Journal of the Chemical Society, Faraday Transactions 1: Physical Chemistry in Condensed Phases*,**78**:545-554.
17. Compton RG, Coles BA, Marken F. Microwave activation of electrochemical processes at microelectrodes. *Chemical Communications* 1998:2595-2596.
18. Gründler P, Flechsig GU. Deposition and stripping at heated microelectrodes. Arsenic(V) at a gold electrode. *Electrochimica Acta* 1998,**43**:3451-3458.
19. Baranski AS. Hot microelectrodes. *Analytical Chemistry* 2002,**74**:1294-1301.
20. Macdonald DD, Engelhardt G, Garcia KM. Development of advanced in-situ techniques for chemistry monitoring and corrosion mitigation in SCWO

- environments. 1998 annual progress report. In; 1998. pp. Medium: ED; Size: 3 pages.
21. Macdonald DD, Wentrczek PR, Scott AC. The measurement of pH in aqueous systems at elevated temperatures using palladium hydride electrodes. *Journal of the Electrochemical Society* 1980,**127**:1745-1751.
  22. Allen J. Bard LRF. Electrochemical Methods, Fundamentals and Applications. In: John Wiley and Sons; 2000.
  23. Banks CE, Simm AO, Bowler R, Dawes K, Compton RG. Hydrodynamic Electrochemistry: Design for a High-Speed Rotating Disk Electrode. *Analytical Chemistry* 2005,**77**:1928-1930.
  24. Lindgren A, Munteanu F-D, Gazaryan IG, Ruzgas T, Gorton L. Comparison of rotating disk and wall-jet electrode systems for studying the kinetics of direct and mediated electron transfer for horseradish peroxidase on a graphite electrode. *Journal of Electroanalytical Chemistry*,**458**:113-120.
  25. Compton RG. *Understanding Voltammetry*. London: Imperial College Press; 2011.
  26. Wojtowicz J, Conway BE. Construction and operation of a rotating disc electrode for elevated temperatures. *Journal of Electroanalytical Chemistry and Interfacial Electrochemistry* 1967,**13**:333-342.
  27. Trevani LN, Calvo E, Corti HR. Diffusion coefficients of iodide in high temperature aqueous solutions. *Electrochemistry Communications* 2000,**2**:312-316.
  28. Compton RG. hydrodynamic voltammetry. In: University of Cambridge.
  29. Chin DT, Tsang CH. Mass transfer to an impinging jet electrode. *Journal of the Electrochemical Society* 1978,**125**:1461-1470.
  30. Curtiss LA, Halley JW, Hautman J, Hung NC, Nagy Z, Rhee YJ, *et al.* Temperature Dependence of the Heterogeneous Ferrous-Ferric Electron Transfer Reaction Rate: Comparison of Experiment and Theory. *Journal of The Electrochemical Society* 1991,**138**:2032-2040.

31. Balashov VN, Fedkin MV, Lvov SN. Experimental system for electrochemical studies of aqueous corrosion at temperatures above 300°C. *Journal of the Electrochemical Society* 2009,**156**:C209-C213.
32. Itagaki M, Fujimura Y, Shitanda I, Watanabe K, Hachiya T. Evaluation of the oxygen reduction activities of rare-earth oxide-supported silver catalysts using a channel flow double electrode. *Analytical Sciences* 2006,**22**:1315-1318.
33. Wakabayashi N, Takeichi M, Itagaki M, Uchida H, Watanabe M. Temperature-dependence of oxygen reduction activity at a platinum electrode in an acidic electrolyte solution investigated with a channel flow double electrode. *Journal of Electroanalytical Chemistry*,**574**:339-346.
34. Snowden ME, King PH, Covington JA, Macpherson JV, Unwin PR. Fabrication of Versatile Channel Flow Cells for Quantitative Electroanalysis Using Prototyping. *Analytical Chemistry* 2010,**82**:3124-3131.
35. Tam KY, Wang RL, Lee CW, Compton RG. Applications of the channel flow cell for UV-visible spectroelectrochemical studies: The kinetics of dimerization of the methyl viologen radical cation. *Electroanalysis* 1997,**9**:219-224.
36. Barbour R, Wang Z, Bae IT, Tolmachev YV, Scherson DA. Channel Flow Cell for Attenuated Total Reflection Fourier Transform Infrared Spectroelectrochemistry. *Analytical Chemistry* 1995,**67**:4024-4027.
37. Marley NA, Ott M, Fearey BL, Benjamin TM, Rogers PSZ, Gaffney JS. High-temperature and -pressure system for laser Raman spectroscopy of aqueous solutions. *Review of Scientific Instruments* 1988,**59**:2247-2253.
38. Macdonald DD, Scott AC, Wentrcek P. Redox potential measurements in high temperature aqueous systems. *Journal of the Electrochemical Society* 1981,**128**:250-257.
39. Engelhardt GR, Lvov SN, Macdonald DD. Importance of thermal diffusion in high temperature electrochemical cells. *Journal of Electroanalytical Chemistry*,**429**:193-201.



40. Compton RG, Fisher AC, Wellington RG, Dobson PJ, Leigh PA. Hydrodynamic voltammetry with microelectrodes: channel microband electrodes; theory and experiment. *The Journal of Physical Chemistry* 1993,**97**:10410-10415.
41. Cooper JA, Compton RG. Channel Electrodes — A Review. *Electroanalysis* 1998,**10**:141-155.
42. Santillo M, Ewing A, Heien M. Trends in computational simulations of electrochemical processes under hydrodynamic flow in microchannels. *Analytical and Bioanalytical Chemistry* 2011,**399**:183-190.
43. Cutress IJ, Dickinson EJJ, Compton RG. Analysis of commercial general engineering finite element software in electrochemical simulations. *Journal of Electroanalytical Chemistry* 2010,**638**:76-83.
44. Dickinson EJJ, Ekström H, Fontes E. COMSOL Multiphysics®: Finite element software for electrochemical analysis. A mini-review. *Electrochemistry Communications* 2014,**40**:71-74.
45. Klymenko OV, Gavaghan DJ, Harriman KE, Compton RG. Finite element simulation of electrochemically reversible, quasi-reversible and irreversible linear sweep voltammetry at the wall tube electrode. *Journal of Electroanalytical Chemistry* 2002,**531**:25-31.
46. Ebrahimi Khabbazi A, Richards AJ, Hoorfar M. Numerical study of the effect of the channel and electrode geometry on the performance of microfluidic fuel cells. *Journal of Power Sources* 2010,**195**:8141-8151.
47. Amatore C, Lemmer C, Sella C, Thouin L. Channel Microband Chronoamperometry: From Transient to Steady-State Regimes. *Analytical Chemistry* 2011,**83**:4170-4177.
48. Wang Z, Zhao M, Scherson DA. Channel Flow Cell For UV/Visible Spectroelectrochemistry. *Analytical Chemistry* 1994,**66**:4560-4563.
49. Rees NV, Dryfe RAW, Cooper JA, Coles BA, Compton RG, Davies SG, *et al.* Voltammetry under High Mass Transport Conditions. A High Speed Channel Electrode for the Study of Ultrafast Kinetics. *The Journal of Physical Chemistry* 1995,**99**:7096-7101.

50. Rees NV, Alden JA, Dryfe RAW, Coles BA, Compton RG. Voltammetry Under High Mass Transport Conditions. The High Speed Channel Electrode and Heterogeneous Kinetics. *The Journal of Physical Chemistry* 1995,**99**:14813-14818.
51. Heller-Ling N, Poillerat G, Koenig JF, Gautier JL, Chartier P. Double channel electrode flow cell (DCEFC): application to the electrocatalysis of the oxygen reduction on oxide films. *Electrochimica Acta* 1994,**39**:1669-1674.
52. Brett AMC. Design and electrochemical evaluation of an optically transparent thin-layer electrode flow cell. *Electroanalysis* 1992,**4**:911-914.
53. Amatore C, Pebay C, Thouin L, Wang A, Warkocz JS. Difference between Ultramicroelectrodes and Microelectrodes: Influence of Natural Convection. *Analytical Chemistry* 2010,**82**:6933-6939.
54. Trevani L, Ehlerova J, Sedlbauer J, Tremaine PR. Complexation in the Cu(II)-LiCl-H<sub>2</sub>O system at temperatures to 423 K by UV-Visible spectroscopy. *International Journal of Hydrogen Energy* 2010,**35**:4893-4900.
55. Ehlerovaa J, Trevanib L, Sedlbauera J, Ballerat-Busserollesc K, Tremaineb PR. UV-visible Spectroscopic Study on Nitrophenols Ionization Reactions to 225 o C. In: *15th International Conference on the Properties of Water and Steam*; 2008. pp. xx-yy.
56. Hayward TM, Svishchev IM, Makhija RC. Stainless steel flow reactor for supercritical water oxidation: corrosion tests. *The Journal of supercritical fluids* 2003,**27**:275-281.
57. International ASM, Handbook C, American Society for M. Properties and selection nonferrous alloys and special-purpose materials. In. Materials Park, OH: ASM International; 1990.
58. International ASM, Handbook C, American Society for M. Materials selection and Design. In. Materials Park, Ohio: ASM International; 1997.
59. Dieter GE. *ASM handbook. Vol. 20, Vol. 20*. Metals Park: ASM International; 2001.

60. Delgado JM, Orts JM, Pérez JM, Rodes A. Sputtered thin-film gold electrodes for in situ ATR-SEIRAS and SERS studies. *Journal of Electroanalytical Chemistry* 2008,**617**:130-140.
61. Wrbanek JD, Laster KL. Preparation and analysis of platinum thin films for high temperature sensor applications. *NASA/TM-2005-213433* 2005:1-19.
62. Nefedov A, Abromeit A, Morawe C, Stierle. High-resolution x-ray scattering study of platinum thin films on sapphire. *Journal of Physics: Condensed Matter* 1998,**10**:717.
63. Çiftyürek E, Sabolsky K, Sabolsky EM. Platinum thin film electrodes for high-temperature chemical sensor applications. *Sensors and Actuators B: Chemical* 2013,**181**:702-714.
64. Rand MJ. Chemical Vapor Deposition of Thin-Film Platinum. *Journal of The Electrochemical Society* 1973,**120**:686-693.
65. Sugawara Y, Okayasu T, Yadav AP, Nishikata A, Tsuru T. Dissolution mechanism of platinum in sulfuric acid solution. *Journal of The Electrochemical Society* 2012,**159**:F779-F786.
66. Ragimov AV, SadykhZade SI, Suleimanova SS, Liogon'kii BI. Redox properties of polyhydroxyquinones. *Polymer Science U.S.S.R.* 1974,**16**:1413-1419.
67. Razimov AV, Bekmashi FT, Liogon'kii BI. Thermal polymerization of p-benzoquinone. *Polymer Science U.S.S.R.* 1975,**17**:3164-3170.
68. Xu T, Liu Q, Liu Z, Wu J. The Role of Supercritical Water in Pyrolysis of Carbonaceous Compounds. *Energy & Fuels* 2013,**27**:3148-3153.
69. Trevani LN, Roberts JC, Tremaine PR. Copper (II)–Ammonia Complexation Equilibria in Aqueous Solutions at Temperatures from 30 to 250° C by Visible Spectroscopy. *Journal of solution chemistry* 2001,**30**:585-622.
70. Zhao X, Imahori H, Zhan C-G, Sakata Y, Iwata S, Kitagawa T. Resonance Raman and FTIR spectra of isotope-labeled reduced 1, 4-benzoquinone and its protonated forms in solutions. *The Journal of Physical Chemistry A* 1997,**101**:622-631.

71. Ahmed M, Khan ZH. Electronic absorption spectra of benzoquinone and its hydroxy substituents and effect of solvents on their spectra. *Spectrochimica Acta Part A: Molecular and Biomolecular Spectroscopy* 2000,**56**:965-981.
72. Uematsu M, Frank EU. Static Dielectric Constant of Water and Steam. *Journal of Physical and Chemical Reference Data* 1980,**9**:1291-1306.
73. Donachie MJ. *Titanium: A Technical Guide, 2nd Edition*: ASM International; 2000.

## Appendix A: Copy right permission

---

### AIP PUBLISHING LLC LICENSE TERMS AND CONDITIONS

Licensee: Fereshteh Samiee

License Date: Aug 20, 2015

License Number: 3692861208734

Publication: Review of Scientific Instruments

Title: Rotating disk electrode system for elevated pressures and temperatures

Type of Use: Thesis/Dissertation

Total: 0.00 CAD

**All payments must be made in full to CCC. For payment instructions, please see information listed at the bottom of this form.**

License Number 3692861208734

Order Date Aug 20, 2015

Publisher AIP Publishing LLC

Publication Review of Scientific Instruments

Article Title Rotating disk electrode system for elevated pressures and temperatures

Author M. J. Fleige, G. K. H. Wiberg, M. Arenz

Online Publication Date Jun 12, 2015

Volume number 86

Issue number 6

Type of Use Thesis/Dissertation

Requestor type Student

Format Electronic

Portion Figure/Table

Number of figures/tables 1

Title of your thesis / dissertation Design a High Temperature hydrodynamic System

Expected completion date Oct 2015

Estimated size (number of pages) 100

Total 0.00 CAD

Terms and Conditions **AIP Publishing LLC -- Terms and Conditions: Permissions Uses**